

# Holographic Optical Manipulation of Trapped Ions for Quantum Simulation

by

Chung-You Shih

A thesis  
presented to the University of Waterloo  
in fulfillment of the  
thesis requirement for the degree of  
Master of Science  
in  
Physics (Quantum Information)

Waterloo, Ontario, Canada, 2019

© Chung-You Shih 2019

## **Author's Declaration**

I hereby declare that I am the sole author of this thesis. This is a true copy of the thesis, including any required final revisions, as accepted by my examiners.

I understand that my thesis may be made electronically available to the public.

## Abstract

Trapped ion is one of the leading platforms for quantum simulation experiment due to its long coherence time and high fidelity state initialization, detection, and manipulation. To individually address ions at a single-ion level, it requires sophisticated optical engineering. In the thesis, we present a novel single qubit addressing system that is immune to imperfections of optical imaging and can scale to different size of the system. The technique is based on digital light processing with a commercially available digital micro-mirror device (DMD).

A DMD is a 2D array that consists of tiny micro-mirrors that can be individually manipulated. It is commonly used in movie projectors to modulate the intensity of the light to create the desired image. However, using this technology to ions will require more sophisticated controls over optical wavefronts of the laser beams, for example, the necessity to manipulate the optical phase. It can be achieved by using the DMD as a programmable hologram, which can then be used to characterize and compensate for any imaging imperfections as well. We developed a new iterative Fourier transform algorithm (IFTA) for calculating the holograms. In the simulation, our algorithm shows more than one order of magnitude improvement in accuracy comparing to previously proposed algorithms. We experimentally demonstrated this holographic beam shaping technique with the optical aberration being compensated. The laser we used in the experiment is in the ultraviolet (UV) regime that is close to the optical transition used for manipulating  $^{171}\text{Yb}^+$  qubits. The short wavelength makes it more susceptible to environmental disturbance.

Also, we proposed and experimentally demonstrated a new scheme that enables holographic controls over lights with multiple laser frequencies simultaneously by combing the DMD with an acousto-optical modulator (AOM). The AOM splits the light and illuminates different zones of the DMD. Each zone has its own hologram forming one frequency channel for addressing. This opens the possibility to engineer more complex Hamiltonian for quantum simulation. For example, we can engineer arbitrary spin-spin interaction graphs by applying the Mølmer-Sørensen scheme on this new setup.

## Acknowledgements

First I want to thank my advisor, Dr. Kazi Rajibul Islam, for offering this wonderful and unique opportunity to be one of his first graduate students participating in the research in the Quantum Information with Trapped Ions group (QITI Lab). He is an amazing advisor. It is lucky for me to have his support, and I always enjoy the time of discussing physics with him.

I want to thank my advisory committee and thesis committee, Dr. Thomas Jennewein, Dr. Michal Bajcsy, and Dr. Kevin Resch, for their valuable advice on my research. It is their valuable suggestions make this works better. I also want to thank Professor Dr. Crystal Senko for her amazing lectures on trapped ions. This course is a great aid in helping me get into this field.

I want to thank my wonderful colleagues, Nikhil, Sainath, Nikolay, Kaleb, Fereshteh, Roland in QITI Lab and Rich, Brendan, Pei Jiang, Noah, Matt from Dr. Senko's group.group. It is an amazing experience to build the lab from scratch with them, and I always learned a lot from all our energetic discussions. I would like to thank all my friends here or in Taiwan My life as a master student will not be as happy as it is without them.

Last but not least, I would like to express my gratitude to my families, especially my parents. It is their support that makes me able to be here and pursue my dream.

## **Dedication**

This is dedicated to those I love.

# Table of Contents

<b>1</b>	<b>Introduction to trapped ion quantum simulation</b>	<b>1</b>
1.1	Trapped ion qubit preparation . . . . .	2
1.2	Interaction in trapped ions system . . . . .	5
1.3	Thesis Outline . . . . .	7
<b>2</b>	<b>Holographic Beam Shaping for Quantum Simulation</b>	<b>8</b>
2.1	Individual Addressing . . . . .	8
2.2	Fourier Holography . . . . .	11
2.3	Digital Micro-Mirror Device . . . . .	13
2.4	Off-Axis Amplitude Hologram . . . . .	16
2.5	Binarization . . . . .	18
2.6	Iterative Fourier Transform Algorithm . . . . .	25
2.7	Chapter Summary . . . . .	29
<b>3</b>	<b>Calibration and Use Cases</b>	<b>30</b>
3.1	Aberration Phase Profile Measurement . . . . .	30
3.2	Aberration Calibration with An Ion . . . . .	34
3.3	Maximizing Diffraction Efficiency . . . . .	35
3.4	Use case: Linear Gradient Intensity . . . . .	37
3.5	Chapter Summary . . . . .	41

<b>4</b>	<b>Holographic Addressing with Multiple Frequency Channels</b>	<b>43</b>
4.1	Frequency Channels Preparation . . . . .	45
4.2	Experiment Results . . . . .	48
4.3	Chapter Summary . . . . .	51
<b>5</b>	<b>Summary and Outlook</b>	<b>53</b>
	<b>References</b>	<b>55</b>
	<b>APPENDICES</b>	<b>58</b>
<b>A</b>	<b>Branching Ration of D1 and D2 Line in <math>^{171}\text{Yb}^+</math></b>	<b>59</b>
<b>B</b>	<b>Holographic Beam Shaping with Pulsed Laser</b>	<b>62</b>

# Chapter 1

## Introduction to trapped ion quantum simulation

Quantum computation has the potential to fundamentally change our society, from breaking standard encryption algorithms [18] to accelerating machine learning techniques [1]. While a large-scale quantum computer is perhaps years away, moderately sized special-purpose computing machines, called quantum simulators are already useful in solving problems in quantum many-particle physics and quantum chemistry. Quantum simulators have the potential to shed light on the origin of high-temperature superconductivity, to discover new phases of matter, and to find new drug molecules.

Long coherence times[22], high fidelity qubit state initialization and detection, and programmable long-range interactions make trapped ions a leading platform for quantum simulation. The trapped ions that are commonly used in quantum simulation or computation experiment are usually from alkali earth metal elements or other elements also having two valence electrons. After ionization, an ion will have only one valence electron providing a relatively simple hydrogen-like electronic state structure. To use a trapped ion as a quantum bit (qubit), we usually pick two electronic states as  $|0\rangle$  and  $|1\rangle$ . Depending on the states and the ions one picked, there are currently two schemes of storing quantum information in an ion. As shown in figure 1.1, the ion qubit is manipulated through a narrow-linewidth optical transition. We called this type of qubit “optical qubit”, for example,  $^{40}\text{Ca}^+$ [16]. For  $^{40}\text{Ca}^+$ , the  $S_{1/2}$  and  $D_{5/2}$  states are usually used for encoding quantum information. The two states are coupled with a dipole-forbidden quadruple transition at 729 nm.



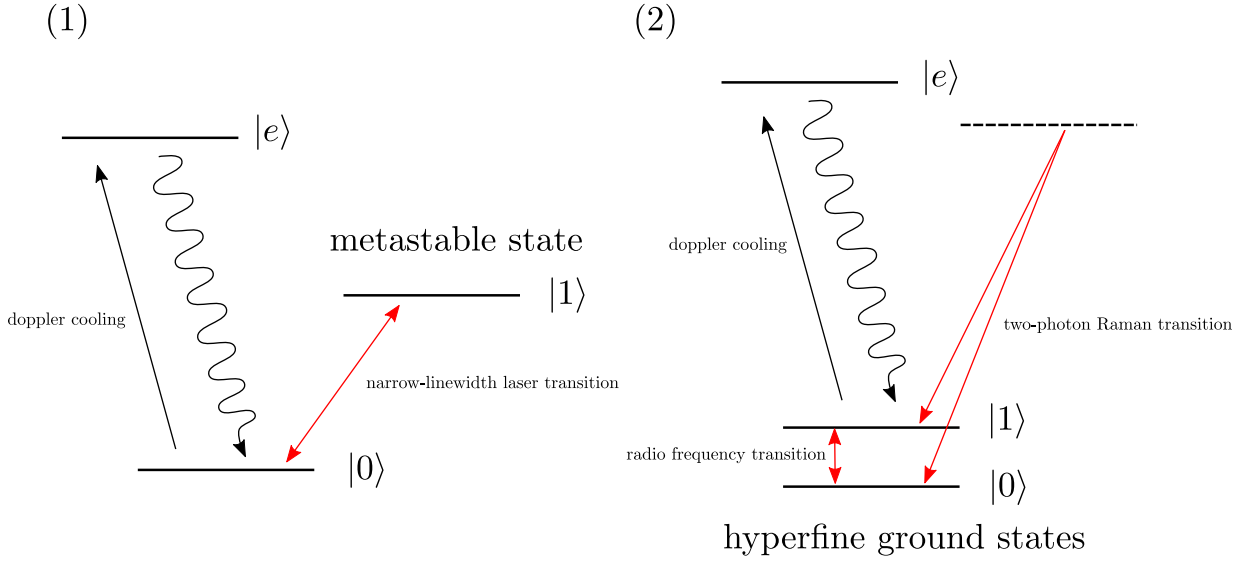


Figure 1.1: Energy diagram of the optical qubits and the hyperfine qubits. (1) Optical qubits (2) Hyperfine qubits

As for the other scheme, it uses two hyperfine ground states as its qubit states. The qubit can be manipulated with microwave or a two-photon Raman transition. This kind of qubit is referred to as “microwave qubit” or “hyperfine qubit”. In our laboratory, we are building a trapped ion quantum simulator using  $^{171}\text{Yb}^+$  which belongs to this type. The two hyperfine ground states  $|F = 0, m_F = 0\rangle$ ,  $|F = 1, m_F = 0\rangle$  are used as the qubit states. This species of ions has been demonstrated to have more than 10 minutes single-ion coherence time [25] and accessible energy states with commercial lasers, making it an ideal choice for quantum simulation experiment.

A typical quantum simulation experiment consists of several stages, including the qubit preparation, the Hamiltonian simulation, and the state detection. In this chapter, we will have brief introductions of each step.

## 1.1 Trapped ion qubit preparation

The very first step of preparing trapped Ytterbium ion qubits for quantum simulation or computation experiment is to ionize neutral Ytterbium atoms and trap them with electric fields.

The source of neutral Ytterbium atoms is typically from an atomic oven. By heating the Ytterbium sample in the atomic oven, the collimated vaporized Ytterbium beam emitted from the oven will pass through the center of the trap. The atomic beam will subsequently be photo-ionized in the trap.

To photoionize the neutral Ytterbium atoms, we use a two-photon process. There are two beams involved. The first one is a frequency-locked laser beam at 399 nm (first ionization beam) which drives a  $^1S_0 \rightarrow ^1P_1$  transition of the neutral Ytterbium atom. The second beam does not have to be a coherent light source. As long as the wavelength of the photon is less than 394 nm[2], the photon will have enough energy to bring the valence electron from  $^1P_1$  excited state to the continuum. In practice, we use the existing beams at 369 nm used for laser cooling which we will describe later. We usually choose the beam direction of the first ionization beam to be perpendicular to the direction of the atomic beam. This setup minimizes the effect of Doppler broadening and enables isotope-selective ionization.

Once the Ytterbium atoms have been ionized, they see the trapping potential created by the static and time-averaged RF electric fields in our Paul trap[14]. A laser beam at 369.5 nm provides Doppler cooling to ions[5]. The ions lose kinetic energy and are trapped. Earnshaw's theorem states that there are no local maximum or minimum points of electric potential in free space. As a result, we combine the static electric field with a fast varying RF electric field to form an equivalent trapping potential in radio-frequency or Paul trap.

When the temperature is low enough, the ions will be crystallized into a 1D chain configuration as figure 1.2 shows. The transition we used for laser cooling is  $^2S_{1/2} \rightarrow ^2P_{1/2}$  transition which corresponds to 369 nm wavelength. The laser frequency of the cooling beam is red-detuned from the transition frequency so that the kinetic energy can be removed from the system through spontaneous emission. This transition is also used for qubit state detection and initialization.

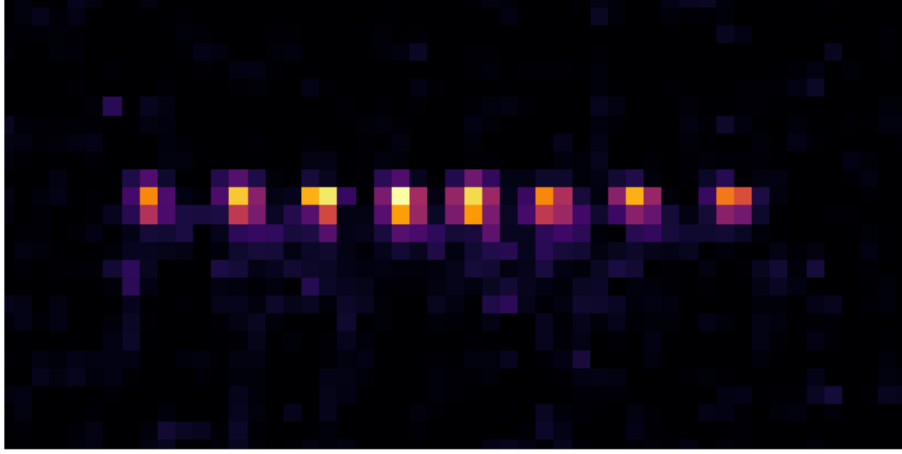


Figure 1.2: A chain of eight  $^{174}\text{Yb}^+$ . The separation between two ions are around  $8\ \mu\text{m}$ .

During the laser cooling process, there is a probability that the ion will fall into the  $^2D_{3/2}$  dark state. Therefore, a repumping beam is required to bring the ions back to the ground state. For Ytterbium ion, the wavelength of the repumping beam is 935 nm which excite the ion to  $^3D[3/2]_{1/2}$  state and decay back to  $^2S_{1/2}$ . Also, another laser beam at 760 nm is required for a similar purpose. It will pump the ions out from the  $^2F_{7/2}$  state which results from the collision between the ions and the residual particles in the chamber. The precise wavelengths of 369 nm, 399 nm, 760 nm, and 935 nm beams differ among different Ytterbium isotopes.

The schematic of the optics in our system is shown in figure 1.3. The electric-optical modulators (EOM) are used to generate sidebands for covering the hyperfine splittings. The acousto-optic modulators (AOM) are used as optical switches. After all the modulation, all the beams will be combined into a polarization-maintaining single photonic crystal fiber (PCF) and be delivered to the ion chain. The PCF has a similar mode field diameters (MFD) from ultraviolet (UV) to near-infrared (NIR) wavelengths. In combination with reflective optics such as off-axis parabolic reflectors, we can have similar beam sizes of all wavelengths at the ion position. The setup greatly simplified the optical alignment near the Vacuum chamber.

## Optical Component Diagram: Cooling + Pumping + Detection

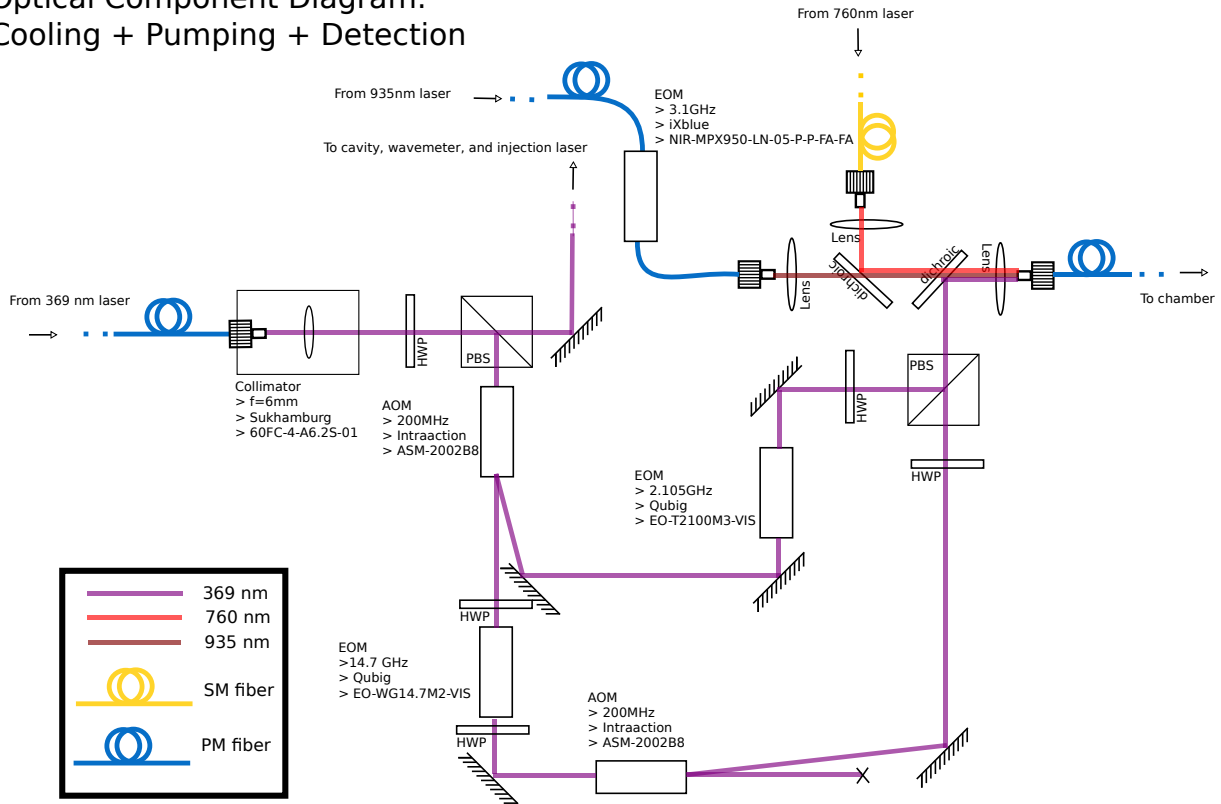


Figure 1.3: The schematic of the optics for trapped ion laser cooling, pumping, and detection beam preparation.

## 1.2 Interaction in trapped ions system

The nature of being charged particles gives ions long-range interactions through Coulomb interactions. In a crystallized ion chain configuration, the Coulomb interactions act as “springs” connecting ions and permit phonons of different collaborative vibrational modes. By introducing spin-dependent forces to the system, we can have phonon mediated spin-spin interactions. The spin-dependent force for  $^{171}\text{Yb}^+$  hyperfine qubits is usually implemented with a Raman transition that couples the internal spin states and vibrational states. As figure 1.4 (a) shows, there are two off-resonance beams involved in the Raman transition. The beat-node frequency matches the energy separation between two spin-vibration states, and the two Raman beams coherently coupled two states. We usually refer to the

transition that couples to a higher phonon number state as blue sideband transition and the transition coupling to a lower phonon number state as red sideband transition.

To engineer a tunable spin-spin coupling or entanglement through optical spin-dependent forces, people have proposed several schemes [3, 19], and the Mølmer-Sørensen scheme is one of the most widely used schemes. The Mølmer-Sørensen scheme consists of two off-resonance Raman transitions. As figure 1.4 (b) shows, an off-resonance red sideband transition and an off-resonance blue sideband transition with beat-node frequency  $\nu_{qubit} - \mu$  and  $\nu_{qubit} + \mu$  are used. Both of the transitions are detuned from the vibrational state so that they will not excite the phonon states directly. Instead, the two transitions coherently couples the spin states ( $|00\rangle$  with  $|11\rangle$ , and  $|10\rangle$  with  $|01\rangle$ ). The Mølmer-Sørensen scheme induces effective Ising spin-spin interactions between every pair of ions which has the following form.

$$H_{eff} = H_{XX} = \sum_{i>j} J_{i,j} S_i^x S_j^x \quad (1.1)$$

$$J_{i,j} = \Omega_i \Omega_j \left( \frac{\hbar \Delta k^2}{2m} \right) \sum_k \frac{b_i^k b_j^k}{\mu^2 - \omega_k^2} \quad (1.2)$$

$\Omega_i$  is the Rabi frequency of the laser addressed on the  $i$ th ion, and  $b_k$  is the eigen vector of a normal mode with frequency  $\omega_k$ . The Rabi frequency is basically proportional to the amplitude of the laser which is square root of the intensity.

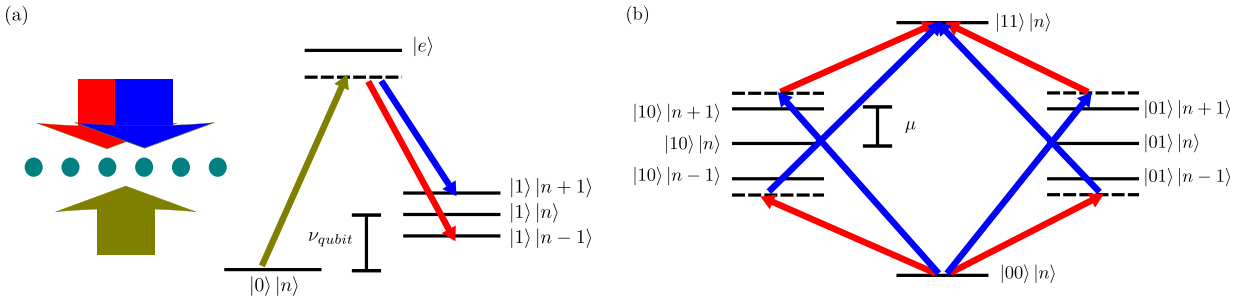


Figure 1.4: (a) Raman transitions of red-sideband and blue-sideband transitions. (b) The Mølmer-Sørensen scheme consists of two off-resonance Raman transitions (red and blue arrows).

The interaction Hamiltonian can be described as a graph. A node in the graph represents an ion qubit, and an edge represents  $J_{i,j}$  which is the interaction strength between the

$i$ th and the  $j$ th ions. In the equation 1.2, it shows if we have full control on the intensity of the light addressed on each ion, we can have the degrees of freedom of equal to the number of ions  $N$ . To have full control of the spin-spin interaction graph which requires  $\frac{N(N-1)}{2}$  degrees of freedom (number of  $J_{i,j}$ ), we need at least  $\lceil \frac{N-1}{2} \rceil$  pairs of Raman beams (red sideband and blue sideband) with different detunings.

An analog way to engineer an arbitrary  $J_{i,j}$  matrix is provided in Korenblit et al (2012)[10].  $J_{i,j}$  can also be controlled without requiring full local optical control of ions in a hybrid analog-digital quantum simulation scheme [15]. However, both of the two methods require precise optical control of ions at the level of individual ions.

## 1.3 Thesis Outline

As we have shown in the previous section, individual addressing is a pivotal technique for engineering a more sophisticated spin-spin interaction graph. However, optical engineering to achieve individual addressing can be very challenging because the separation between ions in a trapped quantum simulator is only a few micrometres. Any imperfections in the addressing system will directly contribute to the error in the interaction Hamiltonian. In the thesis, we will introduce our novel solution, using holographic beam shaping, a technique that uses a re-programmable hologram to engineer the beam profile addressed on the ion chain. Holographic optical manipulation has previously been employed in experiments with neutral atoms[26]. However, ion experiments require working with ultra-violet (UV) wavelength, where aberrations and power efficiency play important roles.

1. Chapter 2: We will introduce our newly developed technique for individual addressing. The new technique harnesses the power of re-programmable holograms, making it immune to optical perfection and can be adapted to different system size.
2. Chapter 3: The experimental considerations, including power efficiency and aberration compensation, will be introduced in this chapter. Along with that, we will also introduce a use case that can be useful in simulating 2D lattice.
3. Chapter 4: As for the frequency control for exciting different modes in the Mølmer-Sørensen scheme, we will introduce a novel protocol that incorporates the frequency control into the holographic beam shaping system in this chapter.
4. Chapter 5: Last, we will discuss our plans in the outlook for integrating the holographic addressing system to our ion trap.

# Chapter 2

## Holographic Beam Shaping for Quantum Simulation

### 2.1 Individual Addressing

The ability to individually address trapped-ion qubits gives us more tuning knobs for engineering the spin-spin interaction Hamiltonian. There are several existing methods, such as using an acoustic-optical deflector (AOD) or multi-channel acoustic-optical modulator (AOM). However, they all have challenges to overcome. For an AOD, the frequency of each addressing beam is all different. It depends on the deflection angle of the beam, which corresponds to the position of the ion. It limits the usage of using AOD for addressing since frequency control is required for Mølmer-Sørensen scheme.

In contrast, multi-channel AOM[4] does not have this issue. Each channel on the multi-channel AOM maps to different ion qubits. Feeding corresponding RF can control the amplitude, the phase and the frequency of each addressing beam to the channels. Nevertheless, the main challenge of using multi-channel AOM is the scalability. In a typical harmonic trapping potential, the longer the ion chain is, the more non-uniform the spacing between ions becomes. However, the spacing between channels is fixed while being manufactured, making the multi-channel AOM optimized for one system size. Also, the multi-channel AOM is a product that is still in development, and it can be prohibitively expensive for most research groups.

To overcome the issues we mentioned, we propose using a holographic beam shaping scheme[26] for ion addressing. In this method, the beam passes through a re-programmable

hologram. The hologram modulates the beam so the beam profile at the ion positions would change accordingly. By generating the right beam profile, the amplitude and phase of the light on each ion can be engineered. The holographic beam shaping method proposed in the thesis allows spatial control independent of frequency.

In figure 2.1, we make a cartoon schematic comparing three different individual addressing schemes. Because the hologram is re-programmable, we can engineer unequal spacing addressing patterns that can adapt to different size of the ion chain. In combination with an AOM for frequency modulation, we will have controls over the frequencies, amplitude and phase of the addressing beams simultaneously. We will discuss it in section 4. Another advantage of holographic beam shaping is that it is immune to static optical imperfections. By adding a phase profile which is opposite to the aberration phase profile of the optical system, we can compensate the aberration.



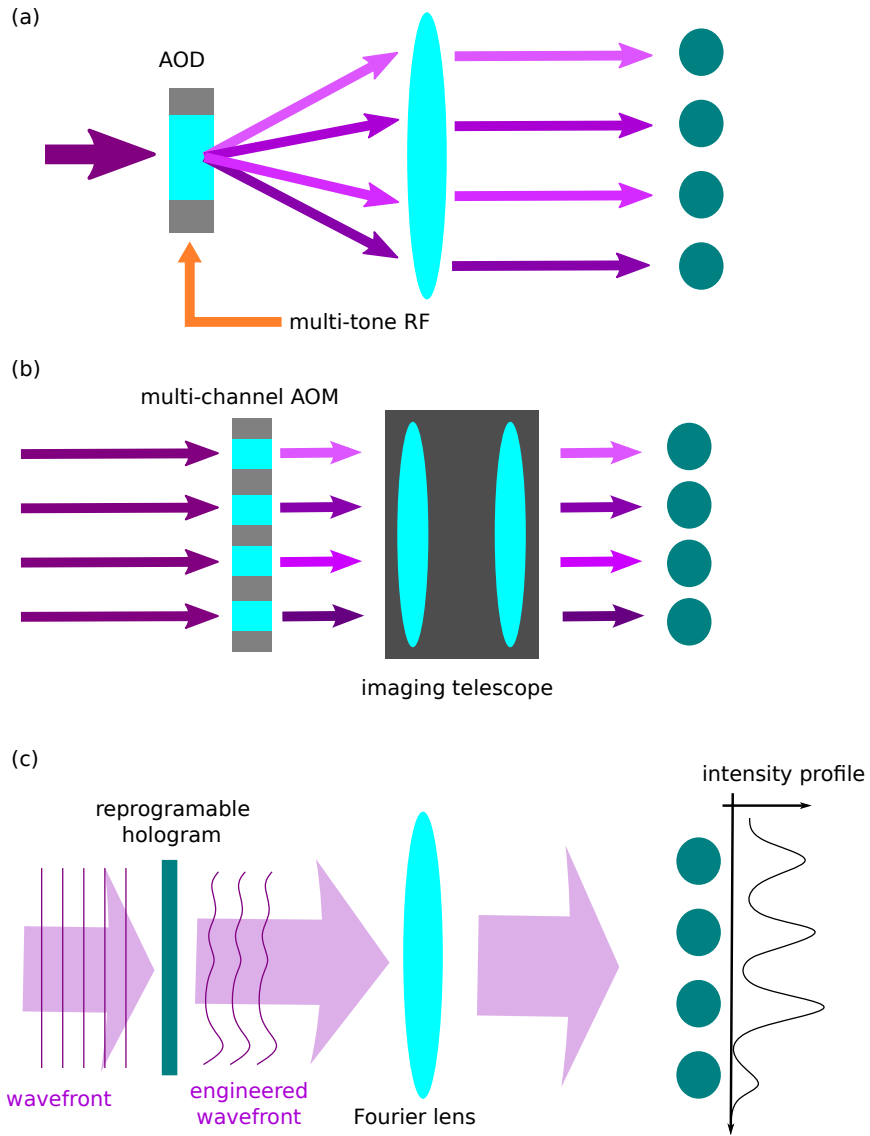


Figure 2.1: Cartoon schematic of comparing three different individual addressing schemes. (a) Use an acoustic-optical deflector (AOD). The deflection angle after the AOD depends on the input RF frequency. (b) Use multi-channel acoustic-optical modulator. The imaging setup maps light coming from each channel to different ions. (c) Holographic beam shaping. (our method) A re-programmable hologram is used to engineer the wavefront of the light making the beam have desired beam profile at the ion position.

## 2.2 Fourier Holography

There are a few different types of holography, such as Fresnel holography, Fourier holography. We use Fourier holography because it works well for creating tiny beam profiles. The basic idea of Fourier holography is that lens performs an optical Fourier transformation on the beams from one of its focal planes to another. To have a better understanding of how the transformation works, we first start with a plane wave. We can write down its time-independent part in the following form.

$$E(x, y, z) = Ae^{i(k_{x0}x+k_{y0}y+k_{z0}z)} \quad (2.1)$$

At the incoming focal plane of the lens where  $z = -f$ , the electric field profile of the beam becomes:

$$E(x, y) = Ae^{i(k_{x0}x+k_{y0}y)}e^{-ik_{z0}f} \quad (2.2)$$

$$= \tilde{A}e^{i(k_{x0}x+k_{y0}y)} \quad (2.3)$$

where we absorb the constant phase term  $e^{-ik_{z0}f}$  into the complex amplitude  $A$  and have it become  $\tilde{A}$ . When a plane wave passes through a thin lens (paraxial lens), it will fall onto one diffraction limited spot. If the aperture is infinity large, the diffraction-limited spot essentially becomes a delta function:

$$E'(x, y) = Be^{ik_{z0}f}\delta^2(x - x_0, y - y_0) \quad (2.4)$$

$$= \tilde{B}\delta^2(x - x_0, y - y_0) \quad (2.5)$$

where  $B$  is the amplitude of the delta function that making it energy conserved. We denote the position of the delta function to be  $(x_0, y_0)$ . Shown in figure 2.2, for a thin lens, we can find the following geometric relationship.

$$\frac{k_{x0}}{k_{z0}} = \frac{x_0}{f} \quad (2.6)$$

$$\frac{k_{y0}}{k_{z0}} = \frac{y_0}{f} \quad (2.7)$$

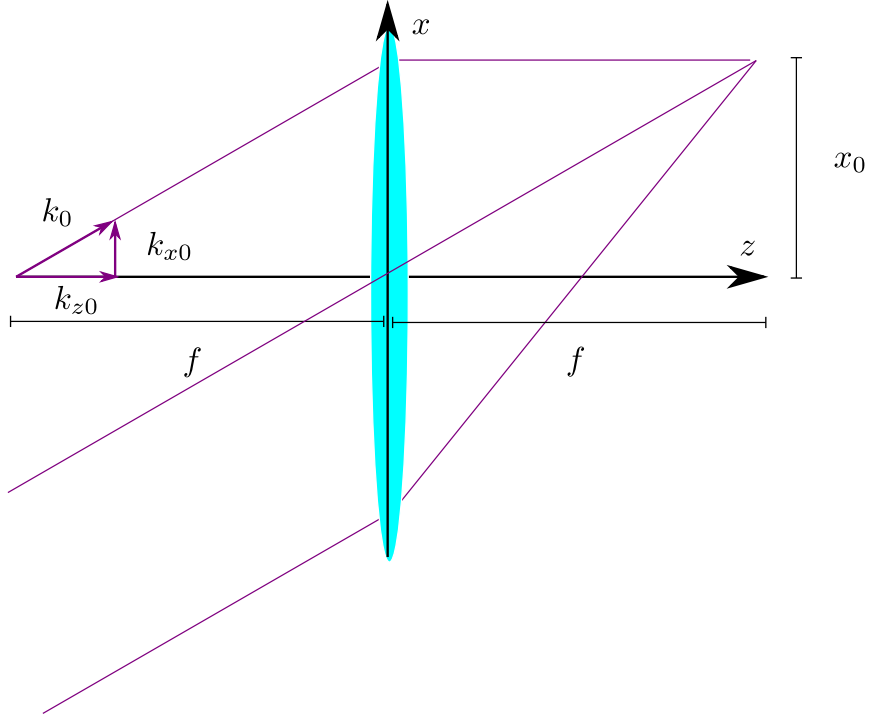


Figure 2.2: Ray tracing of focusing a collimated beam with a thin lens. The lens converts a plane wave on one focal plane to a point (delta function) on the other focal plane. This shows the beam profiles at two focal planes are Fourier conjugate pairs with proper scaling.

To further simplify the expression, here, we make another approximation by assuming the beam is mostly propagating along the  $z$  direction. With the small angle approximation  $k_0 \approx k_{z0}$ , we have:

$$x_0 = \frac{k_{x0}}{k_0} f = \frac{\lambda}{2\pi} f k_{x0} \quad (2.8)$$

$$y_0 = \frac{k_{y0}}{k_0} f = \frac{\lambda}{2\pi} f k_{y0} \quad (2.9)$$

, and thus

$$E'(x, y) = \tilde{B} \delta^2 \left( x - \frac{\lambda}{2\pi} f k_{x0}, y - \frac{\lambda}{2\pi} f k_{y0} \right) \quad (2.10)$$

We can notice that the electric field profiles at the two focal plane,  $E(x, y)$  and  $E'(x, y)$ , are Fourier conjugate pairs with proper scaling (We will show it can be generalized to arbitrary profiles later.).

$$E'(x, y) = \frac{\tilde{B}}{\tilde{A}} \mathcal{F}[E(x, y)](k_x = \frac{2\pi}{\lambda f}x, k_y = \frac{2\pi}{\lambda f}y) \quad (2.11)$$

$$= C e^{i2k_0f} \mathcal{F}[E(x, y)](k_x = \frac{2\pi}{\lambda f}x, k_y = \frac{2\pi}{\lambda f}y) \quad (2.12)$$

. In the equation,  $C$  will be a real normalization constant which make sure the transformation is energy conserved. With Parseval's theorem, we can derive the normalization constant.

$$C = \frac{2\pi}{\lambda f} \quad (2.13)$$

If we ignore the constant phase, we will get the following relation.

$$E'(x, y) = \frac{2\pi}{\lambda f} \mathcal{F}[E(x, y)](k_x = \frac{2\pi}{\lambda f}x, k_y = \frac{2\pi}{\lambda f}y) \quad (2.14)$$

This result can be generalized to arbitrary profiles without any modification. That is due to the fact that any electric field profiles can be decomposed into a sum over a series of plane waves, and Fourier transformation is a linear transformation. For convenience, we will refer the incoming, outgoing focal plane as Fourier plane and image plane respectively throughout the paper. If we deploy a hologram at the Fourier plane and use it to modulate the amplitude and the phase of the electric field at the Fourier plane, we will be able to engineer any desired electric field profile at the image plane.

## 2.3 Digital Micro-Mirror Device

The re-programmable hologram can be implemented with adaptive optics. There are various types of commercially available adaptive optical devices, including liquid-crystal spatial light modulators (LC-SLM)[6], deformable mirrors, and digital micro-mirror devices (DMD)[26]. A significant advantage of using adaptive optics is that they are reconfigurable. We can reprogram the adaptive optics to switch between different holograms to generate various beam profiles.

The adaptive optics we chose is a digital micro-mirror device, DLP9500UV[21] from Texas Instrument. It is controlled by an FPGA-based controller from Visitech. The DMD is a 2D array of micro-mirrors lying on top of a CMOS chip. Each micro-mirror can be individually programmed and tilted to plus and minus twelve degrees along the diagonal

direction as shown in figure 2.4 We can use the DMD to locally turn on or off the reflected light in one direction. Namely, we can do local binary amplitude modulation. Since the micro-mirrors on the DMD are tilted in the diagonal direction, we rotated the whole DMD by 45 degrees for easier optical alignment as the experimental setup shown in figure 2.3. The frame rate of the DMD is more than 10kHz, which is about a hundred times faster than the frame rate of an LC-SLM. That means we can change the quantum operations more frequently since each engineered beam profiles corresponds to a quantum operation we would like to apply on the ions.

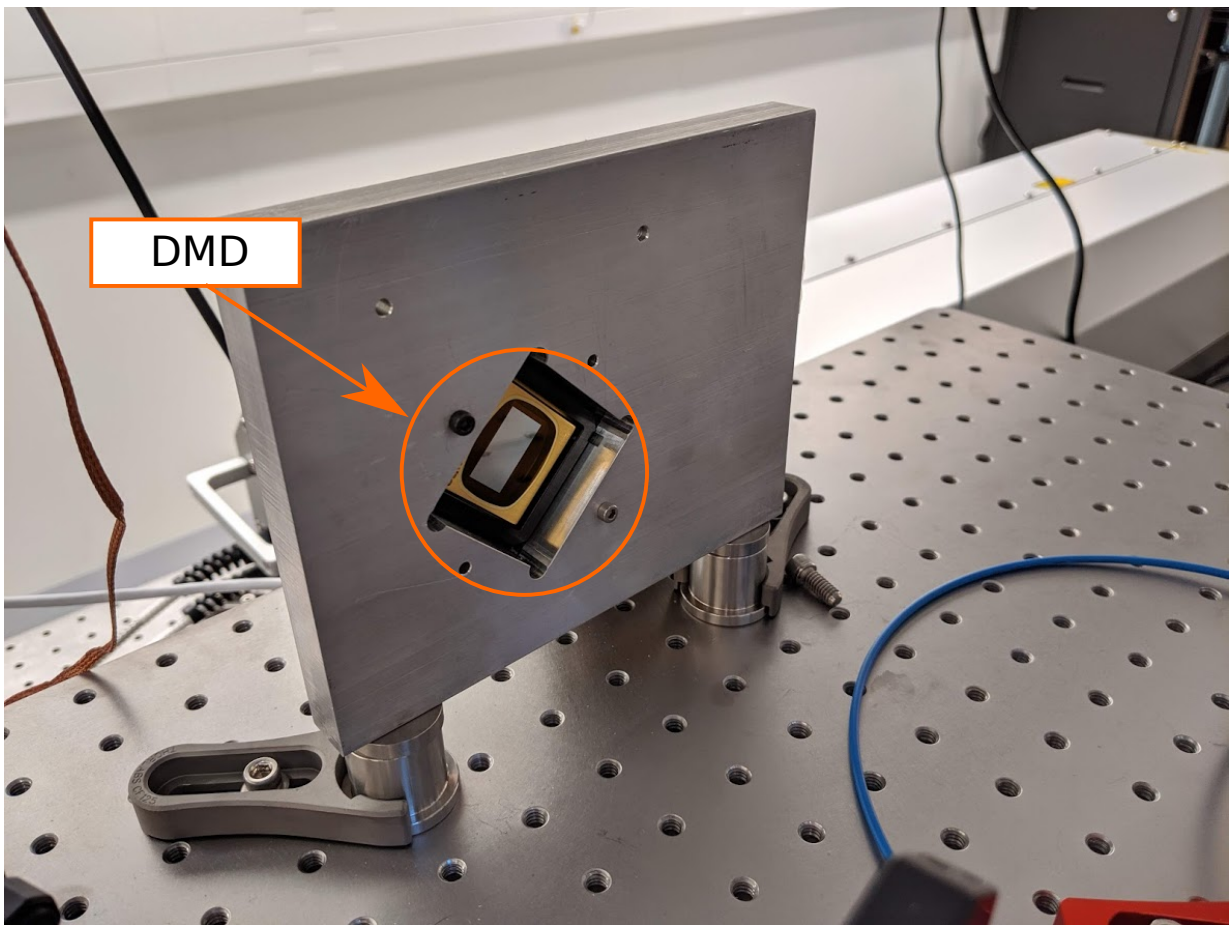


Figure 2.3: The picture of the DMD setup we used in the experiment. The DMD is rotated by 45 degrees due to the fact that the micro-mirror is flipping in the diagonal direction.

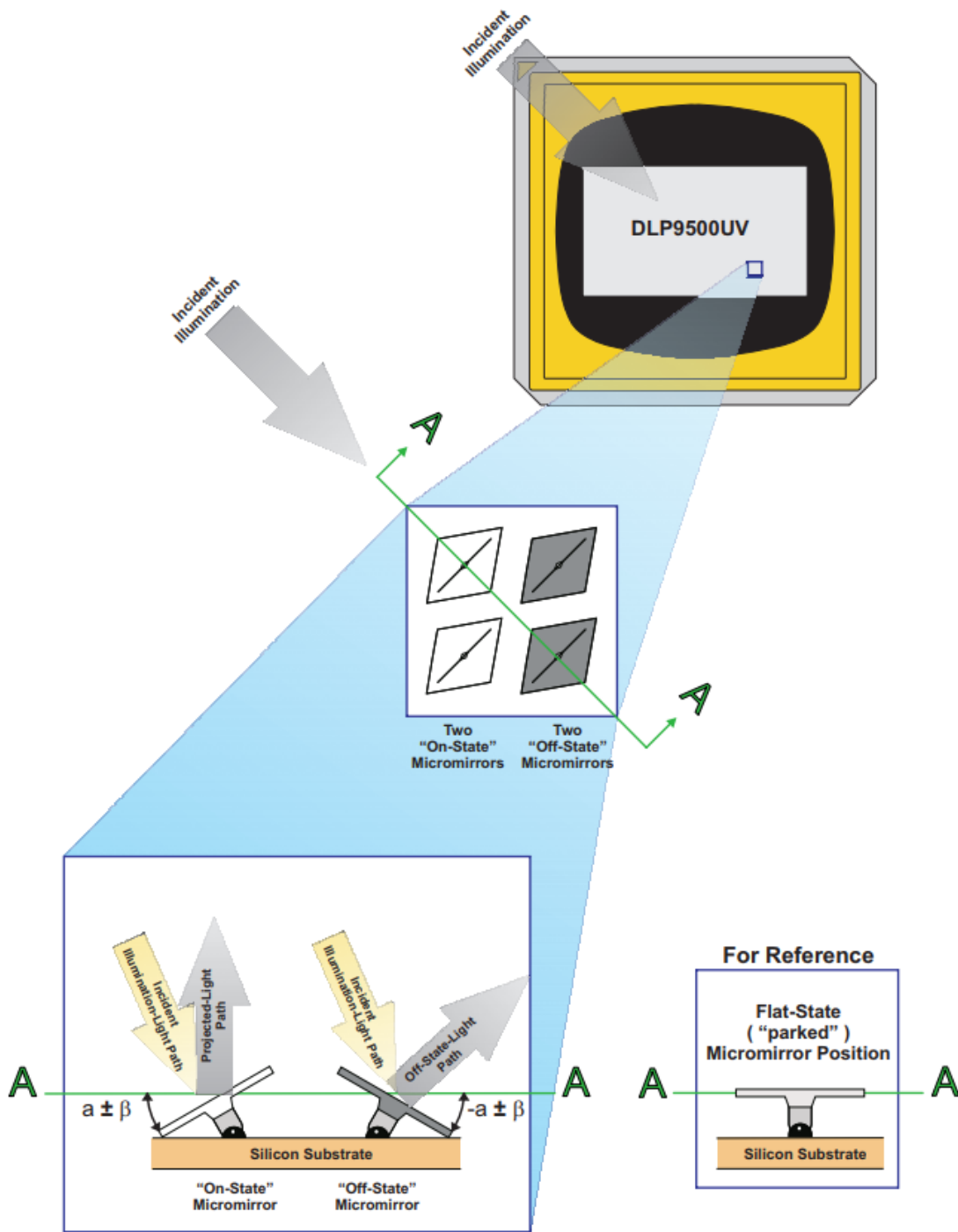


Figure 2.4: Micro-mirror landed positions and light paths. The figure is taken and edited from the DLP9500UV datasheet[21].

## 2.4 Off-Axis Amplitude Hologram

With a DMD, we can have binary local amplitude controls by flipping the micro-mirrors. However, to engineer an arbitrary beam profile at the image plane, we will need some controls on not only the amplitude of the beam profile but also its optical phase.

To understand how we engineer the beam profile with a device that can only do amplitude modulation, let's first relieve the constraint that the amplitude control from the DMD is binary and assume that the device has a continuous (grey scale) amplitude control. Consider we want to engineer a target beam profile  $f(\mathbf{x})$  which has a Fourier conjugate  $F(\mathbf{k})$ .

$$F(\mathbf{k}) = \mathcal{F}[f(\mathbf{x})] \quad (2.15)$$

For simplicity, we use the vector notation,  $\mathbf{x} = (x, y)$  and  $\mathbf{k} = (k_x, k_y)$ .

The idea of using just the amplitude modulation to achieve both amplitude and phase control is through engineering a carrier grating. If we use the diffracted beam from the grating, we will be able to modify the phase of the light by changing the spatial phase of the grating profiles. With this idea in mind, we can implement the amplitude grating function  $G(\mathbf{k})$  with the following form.

$$G(\mathbf{k}) = \frac{|F(\mathbf{k})|}{2} (\cos(\mathbf{x}_0 \cdot \mathbf{k} + \Phi(\mathbf{k})) + 1) \quad (2.16)$$

where

$$\Phi(\mathbf{k}) = \text{Arg}(F(\mathbf{k}))$$

, and  $\mathbf{x}_0$  defines the periodicity of the grating. Note that we add a one to the cos function as the bias to ensure the grating function  $G(\mathbf{k})$  is always positive because the DMD doesn't have the ability to invert the sign of the field (negative value of the grating in equation 2.16). To verify the grating function we just constructed, we can simply apply the inverse Fourier transform.

$$g(\mathbf{x}) = \mathcal{F}^{-1}[G(\mathbf{k})] \quad (2.17)$$

$$= \frac{1}{4} f(\mathbf{x} - \mathbf{x}_0) + \frac{1}{4} f^*(-\mathbf{x} + \mathbf{x}_0) + \frac{1}{2} \mathcal{F}^{-1}[|F(\mathbf{k})|] \quad (2.18)$$

The transformation of the function is consist of three terms, and we refer to the three terms as first, negative first, and zeroth grating order of the beam respectively. We can notice that the first order diffraction beam has the desired beam profile yet with a shifted origin at  $\mathbf{x}_0$ . Because of the shifted-origin nature of the grating-based holograms, holograms of

this type are usually referred to as off-axis holograms. It is worth mentioning that the negative first order is the complex conjugate of the target beam profile. By flipping the sign of  $\Phi(\mathbf{k})$ , we can use the negative first order rather than the first order diffraction beam. Substitute the relation between  $\mathbf{k}$  and  $\mathbf{x}$  (equation 2.8 and 2.9), and we will have:

$$\hat{G}(\mathbf{x}) = \frac{|\hat{F}(\mathbf{x})|}{2} (\cos(2\pi \frac{\mathbf{x}_0 \cdot \mathbf{x}}{\lambda f} + \hat{\Phi}(\mathbf{x})) + 1)$$

Here we add  $\hat{\cdot}$  on top of the function to indicate the substitution.

The grating function we've derived so far requires uniform illumination on the hologram, and the optical aberrations are not taken into account. However, in most of the situation, the light doesn't illuminate the hologram uniformly and suffers from the imperfection of the optics. To address this problem, first, let's denote the beam profile illuminated on the DMD at the Fourier plane to be  $E_{in}(\mathbf{x})$  with aberration phase profile  $\Phi_{in} = \text{Arg}(E_{in})$ . Although the aberrations from DMD itself and the focusing lens are not part of the  $\Phi_{in}$ , we can combine all these aberrations into  $\Phi_{in}$  and thus assume the DMD and the focusing lens will not introduce any optical aberrations. In the later section, we will show how to measure the combined aberrations phase profile for aberration compensation. With some modification, we will be able to get the grating function that can adapt to  $E_{in}$ .

$$\hat{G}(\mathbf{x}) = \eta \left| \frac{\hat{F}(\mathbf{x})}{E_{in}(\mathbf{x})} \right| \frac{1}{2} (\cos(2\pi \frac{\mathbf{x}_0 \cdot \mathbf{x}}{\lambda f} + \hat{\Phi}(\mathbf{x}) - \Phi_{in}(\mathbf{x})) + 1) \quad (2.19)$$

with normalization constant

$$\eta = \max \left( \left| \frac{E_{in}(\mathbf{x})}{\hat{F}(\mathbf{x})} \right| \right) \quad (2.20)$$

to make the value of  $\hat{G}$  between 0 to 1. The beam profile at image plane now becomes:

$$\begin{aligned} E_{img}(\mathbf{x}) &= \frac{2\pi}{\lambda f} \mathcal{F}^{-1} [(E_{in}(\mathbf{x}) \hat{G}(\mathbf{x}))|_{\mathbf{x}=\frac{\lambda f}{2\pi} \mathbf{k}}] \\ &= \frac{2\pi}{\lambda f} \eta \left( \frac{1}{4} f(\mathbf{x} - \mathbf{x}_0) + \frac{1}{4} \mathcal{F}^{-1} [|F(\mathbf{k})| e^{i(-\Phi(\mathbf{k}) + 2\Phi_{in}(\mathbf{x}=\frac{\lambda f}{2\pi} \mathbf{k}))}] (-\mathbf{x} + \mathbf{x}_0) \right. \\ &\quad \left. + \frac{1}{2} \mathcal{F}^{-1} [|F(\mathbf{k})| e^{i\Phi_{in}(\mathbf{x}=\frac{\lambda f}{2\pi} \mathbf{k})}] \right) \end{aligned} \quad (2.21)$$

As we can see in the equation, the first order beam is the aberration-free target beam profile, but the negative first order diffraction suffers two times more aberration.



## 2.5 Binarization

Now we have the method to generate greyscale amplitude holograms that can produce the desired beam profiles. The next step is to binarize the greyscale holograms so that they can be displayed on the DMD. Unfortunately, binarization is a highly nonlinear process, and there is no way to do so without introducing additional error. What we can do is try to find a binary grating function  $G_b(\mathbf{x})$  to approximate the grey scale grating  $G(\mathbf{x})$ . As an example, we show the binarized gratings with different phases and amplitudes in figure 2.5.

The most trivial method to do so is to simply set up a threshold, for example, 0.5, and the value of the binarized hologram is determined by comparing the value of the unbinarized hologram with the threshold. If  $G(\mathbf{x})$  is greater than the threshold,  $G_b(\mathbf{x})$  will be set to 1 which means the micro-mirror flips to the “on” position that will reflect the beam to the lens.

$$G_b(\mathbf{x}) = \begin{cases} 1 & \text{if } G(\mathbf{x}) \geq 0.5 \\ 0 & \text{if } G(\mathbf{x}) < 0.5 \end{cases} \quad (2.22)$$

However, this method gives out a significant amount of localized artifacts. Shown in figure 2.6 is one of the simulation examples we made with this simple threshold method. We can observe artifacts are lying around the target beam profile.

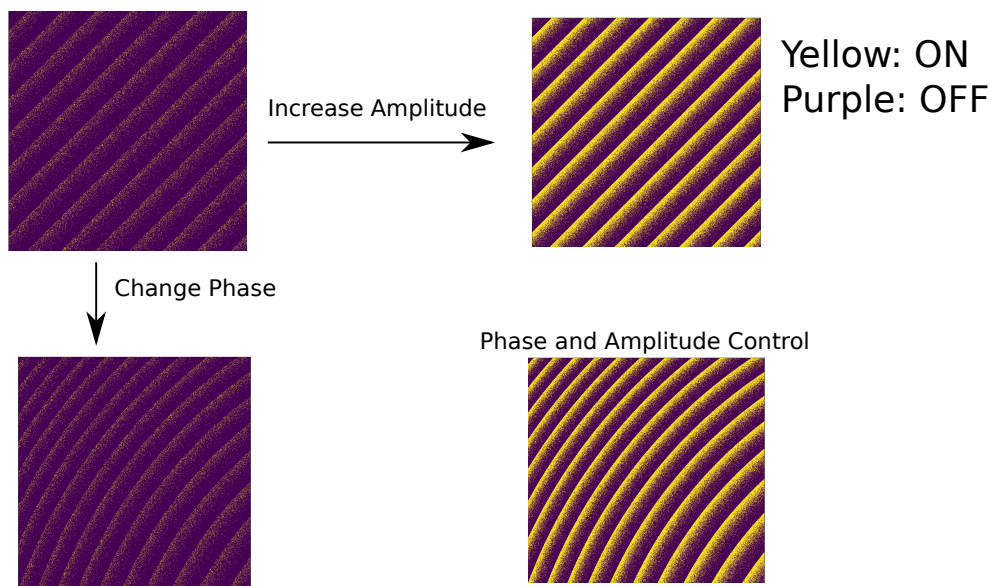


Figure 2.5: Binarized gratings with different phases and amplitudes.

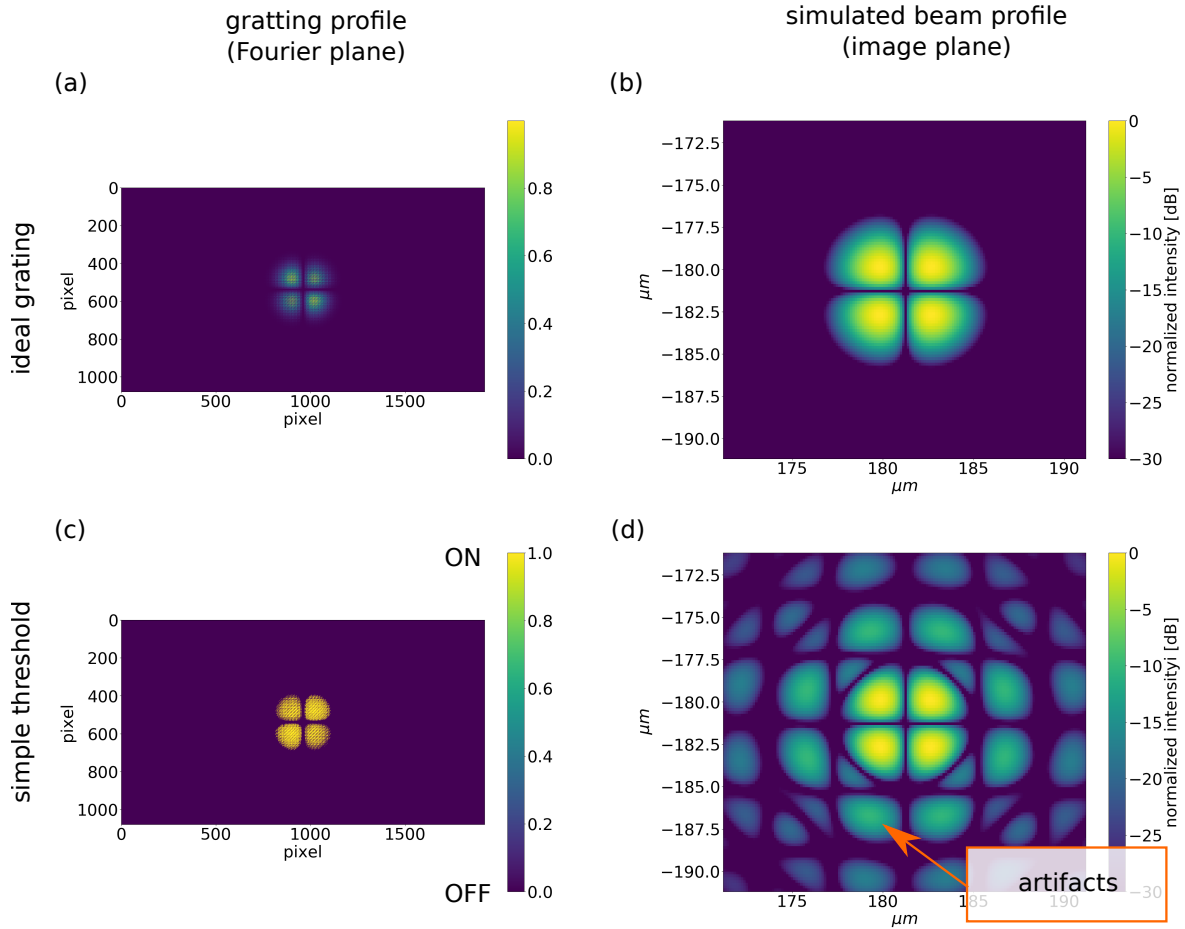


Figure 2.6: Simulation of creating  $\text{TEM}_{11}$  Gaussian beam profile from a fundamental mode Gaussian beam. (a) The ideal grating profile (continuous amplitude modulation). (b) The beam profile at the image plane created with ideal grating hologram. The profile is an ideal  $\text{TEM}_{11}$  Gaussian beam profile. (c) The binarized amplitude grating profile. The binarization is performed with the formula in equation 2.22. (d) The beam profile at the image plane created with the simple threshold method (equation 2.22). One can see artifacts caused the binarization process appear in the image. Simulation condition:  $\lambda = 369 \text{ nm}$ ,  $f = 30\text{mm}$ , grating periodicity = 2 pixel

To mitigate the influence of binarization errors, people have proposed several methods[12, 7, 9, 26]. Shown in figure 2.7 are the simulation results with a hologram calculated with the probabilistic algorithm from [26] and the hologram from 2.19 binarized by an error diffusion

algorithm [8]. We can clearly observe that the artifacts are significantly suppressed.

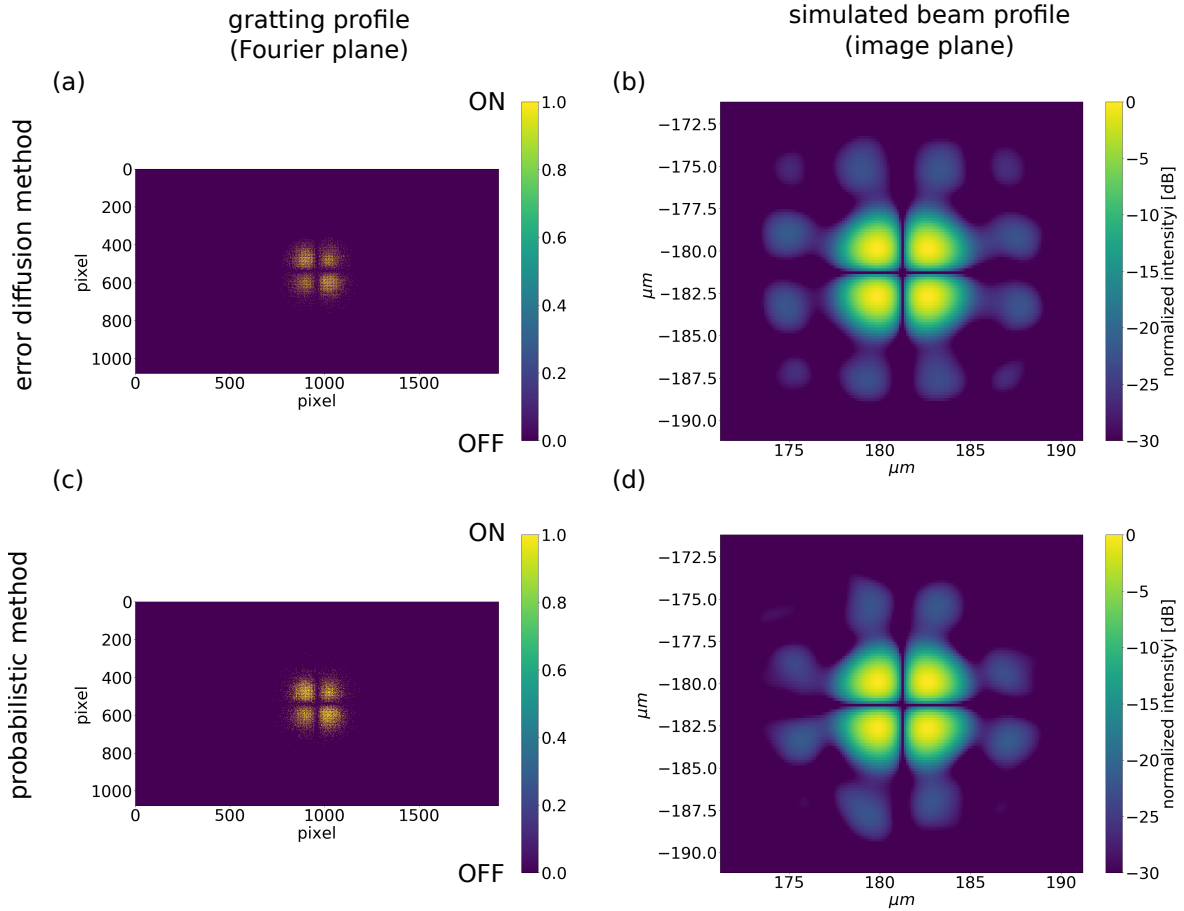


Figure 2.7: Simulation of creating  $TEM_{11}$  Gaussian beam profile from a fundamental mode Gaussian beam with improved binarization methods. (a) The binarized amplitude grating profile created by applying the error diffusion method[8] on the ideal grating. (b) The beam profile at the image plane created with the error diffusion algorithm. (c) The binarized amplitude grating profile created with the probabilistic algorithm from [26] (d) The beam profile at the image plane created with the probabilistic algorithm. Simulation condition:  $\lambda = 369$  nm,  $f = 30$ mm, error diffusion algorithm: Jarvis [8], grating periodicity = 2 pixel

Before going into the details about the binarization and benchmarking the algorithms, we will first discuss what kind of profiles we are interested in. There are multiple ways of

engineering a target beam profile that produces the same quantum gate operation. The beam profile can be arbitrary as long as it has the desired values at the positions ions locate. In other words, we only care about the beam profile close to the region that ions locate. However, in general, we want its optical Fourier transformed profile to have a good overlapping with the input beam profile on the DMD, so more power of the beam can be used in addressing. More specifically, we want to maximize the normalization constant  $\eta$ . Since our input beam profile on the DMD is close to the fundamental Gaussian mode, we made our addressing beam profile a series of Gaussian beams addressed on each ion.

$$E_{target}(\mathbf{x}) = \sum_i a_i e^{|\mathbf{x}-\mathbf{x}_i|^2/w^2} \quad (2.23)$$

Each addressing Gaussian beam satisfies the mode matching condition.

$$w \approx \frac{f\lambda}{\pi w_0} \quad (2.24)$$

where  $w_0$  is the radius of the incoming beam at which the field amplitudes fall to  $1/e$  of their axial values.

To benchmark the performance of the system, we create a beam profile that has equal strength of the light on all ions except one ion in the system. In the small figure at the bottom left of figure 2.8 shows the benchmark pattern we used. As an example, we discuss the accuracy of a six ions system. Hence, we intend to show light with equal intensities at ion  $i = \{1, 2, 3, 4, 6\}$ , while keep ion  $i = 5$  in dark. Therefore, we can define a benchmark metric for the system as:

$$E_{benchmark}(\mathbf{x}) = \sum_{i=\{1,2,3,4,6\}} a e^{|\mathbf{x}-\mathbf{x}_i|^2/w^2} \quad (2.25)$$

We can benchmark the accuracy from the mismatch between peaks. Also, the light leaking to the position of the fifth ion indicates the crosstalk of the system. In figure 2.8, we showed the simulation results with the two algorithms, the probabilistic algorithm and the error-diffusion-based algorithm, along with the unbinned (ideal) version for comparison.

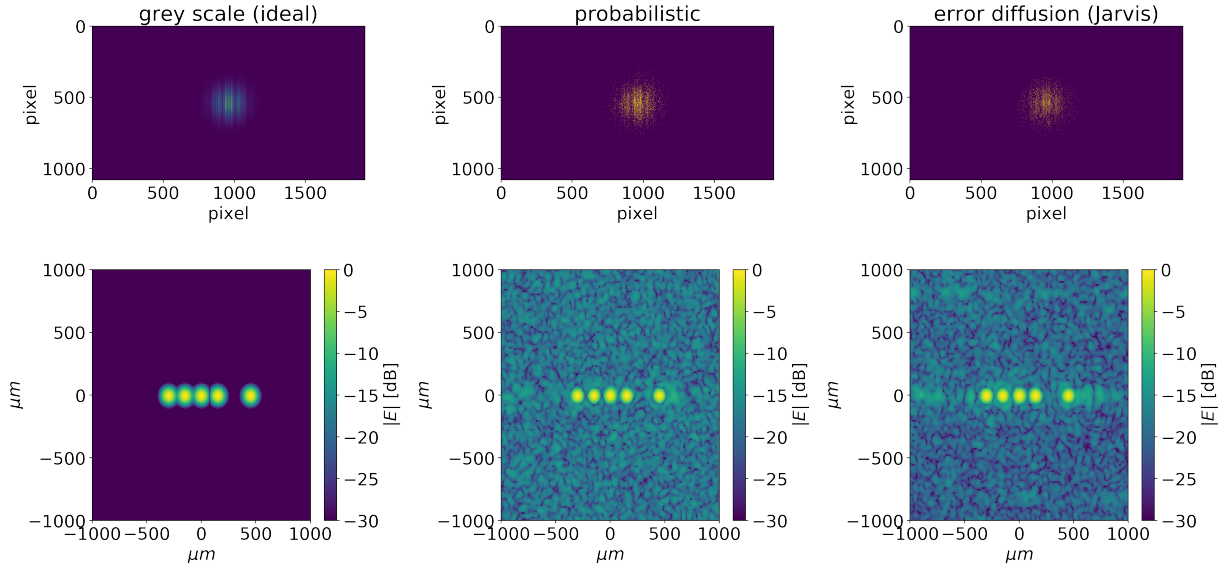


Figure 2.8: Binarization algorithm comparison: The first row shows the grating profile at the Fourier plane, and the second row shows the simulated normalized field amplitude at the image plane. Simulation condition:  $\lambda = 399\text{nm}$ ,  $f = 728\text{ mm}$ , grating periodicity = 2 pixel

To examine the peak mismatch and the crosstalk, we plot the simulation results of the two algorithms in both linear scale and logarithmic scale in figure 2.9 and figure 2.10. The maximum peak mismatch of both of the algorithms is around 5%. As for the crosstalk, the error diffusion method has less crosstalk. It has two to three times less cross talk than that of the probabilistic algorithm. Both of the algorithms may be good enough for creating arbitrary potential in some many-body quantum simulation experiment. However, comparing to the current state-of-the-art experiment [4] which has about 1% (-20dBc) crosstalk in the amplitude, we would like to find a better algorithm.

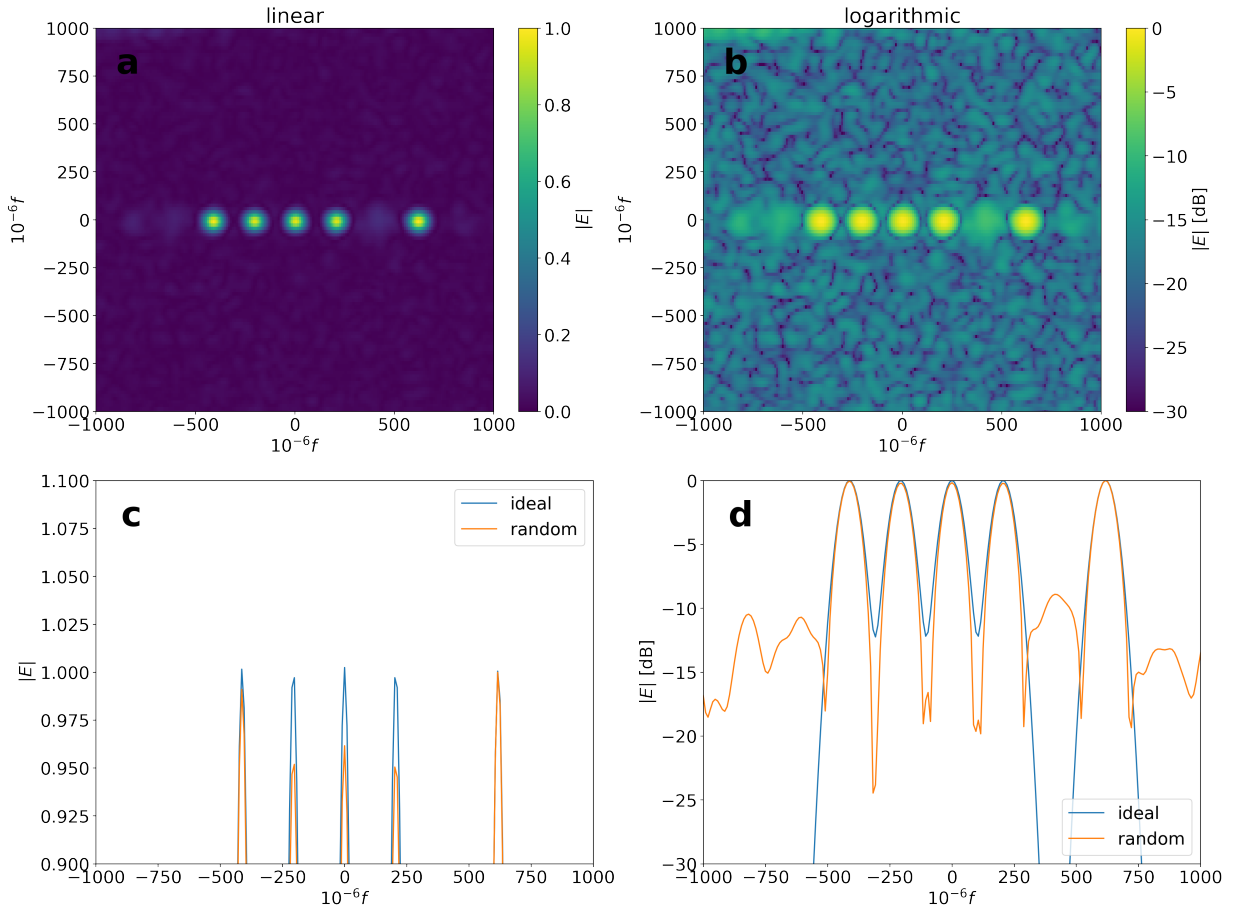


Figure 2.9: Simulation results of beam profile at the image plane with a hologram generated by the probabilistic algorithm[27] (a) Normalized field amplitude. (b) Normalized field Amplitude in the logarithmic scale. (c) Normalized field amplitude of the cross-section along the ion chain direction. (d) Normalized field amplitude of the cross-section along the ion chain direction in the logarithmic scale. (Simulation condition:  $\lambda = 399\text{nm}$ ,  $f = 728\text{ mm}$ , grating periodicity = 2 pixel) There is a maximum 5% peak mismatch shown in figure c and approximately -10 dBc cross-talk in figure d.

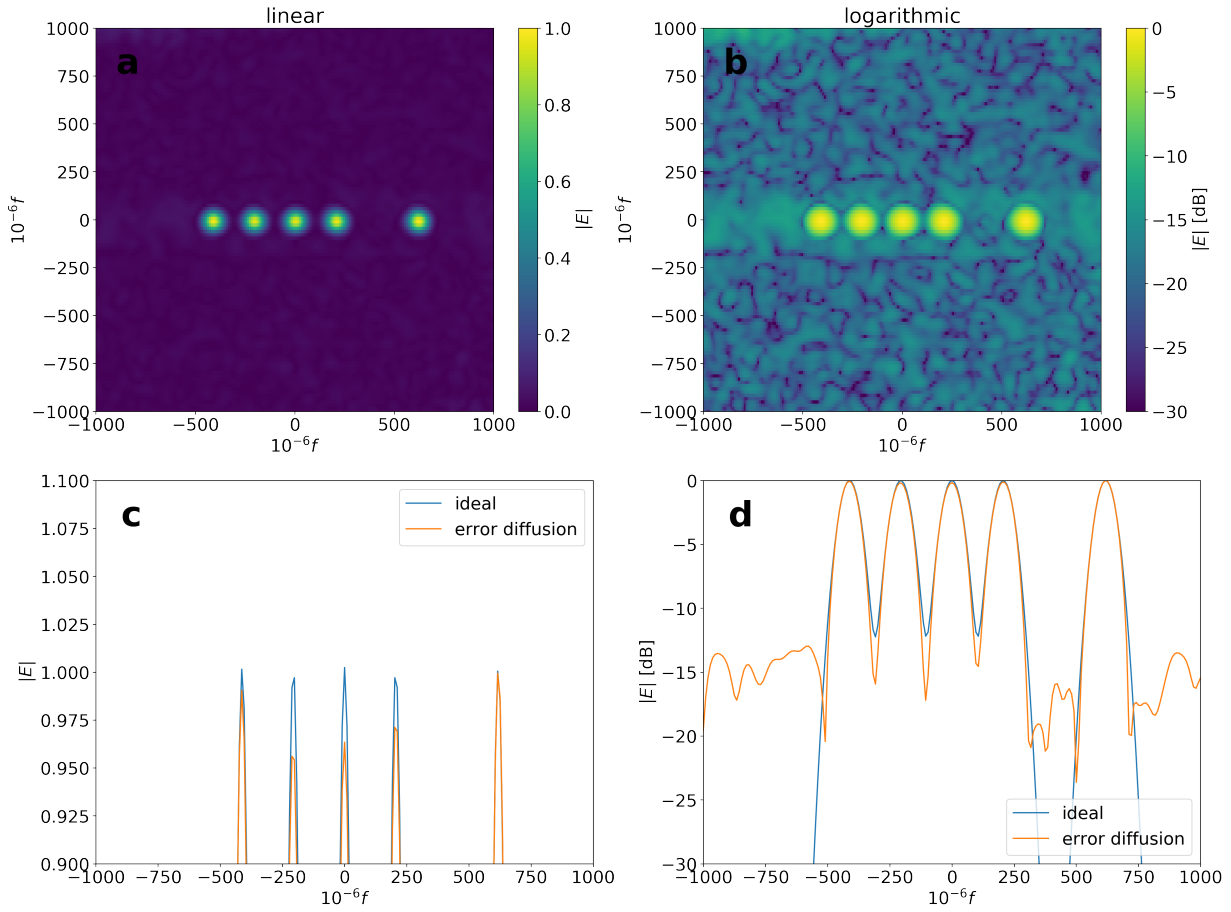


Figure 2.10: Simulation results of beam profile at the image plane with a hologram generated by the error diffusion algorithm (a) Normalized field amplitude. (b) Normalized field Amplitude in the logarithmic scale. (c) Normalized field amplitude of the cross-section along the ion chain direction. (d) Normalized field amplitude of the cross-section along the ion chain direction in the logarithmic scale. (Simulation condition:  $\lambda = 399\text{nm}$ ,  $f = 728\text{ mm}$ , grating periodicity = 2 pixel) There is a maximum 5% peak mismatch shown in figure c and approximately -15 dBc cross-talk in figure d. The cross-talk reduces by about 5 dB comparing to the results in figure 2.9

## 2.6 Iterative Fourier Transform Algorithm

While looking for a better binarization algorithm, one thing we have to keep in mind is the binarization error results from the limited degrees of freedom. Unlike the greyscale hologram which has continuous amplitude control, the DMD has only two states, on and off. Although this means we are not able to get rid of the binarization error completely, we can try to minimize its influence by optimizing the hologram such that within a signal window containing the target beam profile (where the ions locate) the error is minimized. The algorithm we designed to optimize the hologram is an iterative Fourier transform algorithm (IFTA). It is a modification of the binarization algorithm from [24].

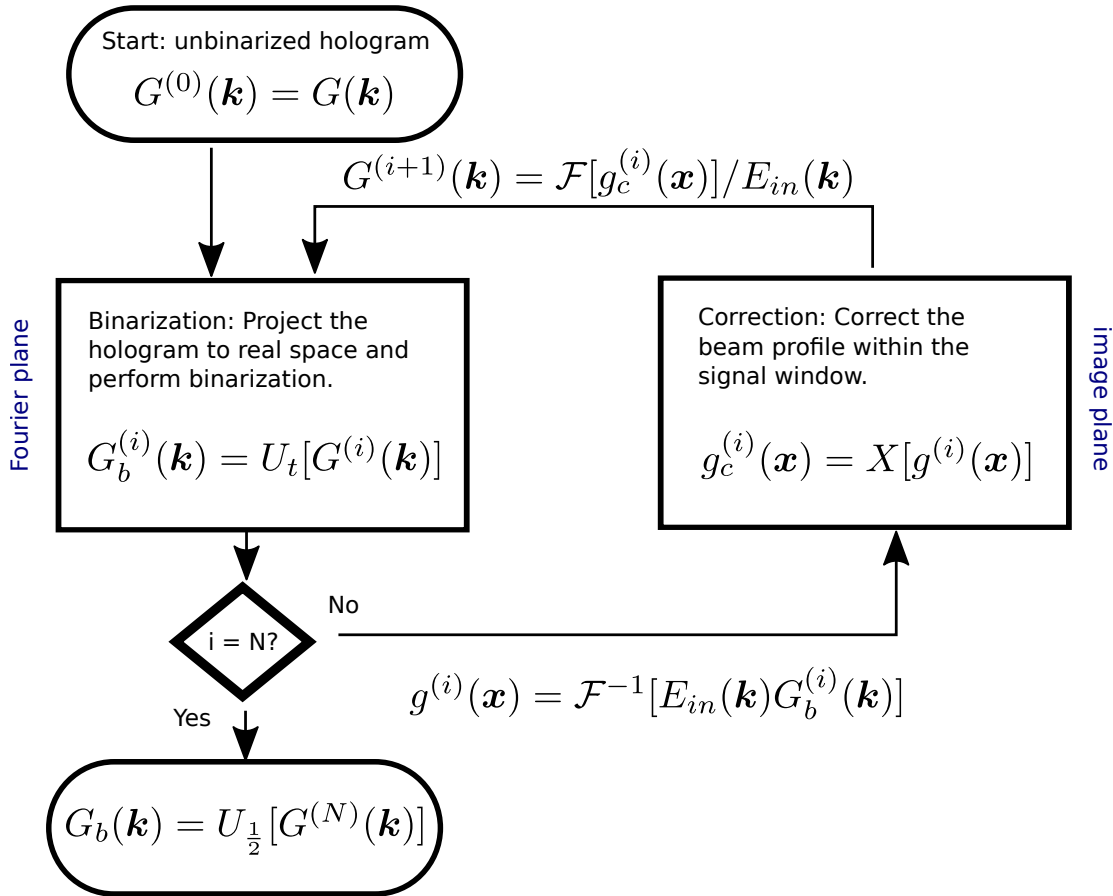


Figure 2.11: The flowchart of our iterative Fourier transform algorithm.



The flow chart of our IFTA is shown in figure 2.11. In the beginning, we start with a greyscale hologram  $G(\mathbf{k})$  and binarized it with a binarization operator  $U$ .

$$G_b^{(1)} = U[G(\mathbf{k})] \quad (2.26)$$

Since we just applied the binarization to the hologram, we will encounter the binarization error when we go from the Fourier plane to the image plane. The next step is to apply a correction operator  $X$  which corrects the beam profile within a signal window  $\mathcal{D}$ . The signal window contains the region we are interested in, for example, the ions.

$$g_c^{(i)}(\mathbf{x}) = X[g^{(i)}(\mathbf{x})] = \begin{cases} g(\mathbf{x}) & \text{if } \mathbf{x} \in \mathcal{D} \\ g^{(i)}(\mathbf{x}) & \text{otherwise} \end{cases} \quad (2.27)$$

where  $g(\mathbf{x})$  is the inverse Fourier transformation of the ideal grating profile. (The target beam profile.)

$$g(\mathbf{x}) = \mathcal{F}^{-1}[G(\mathbf{k})] \quad (2.28)$$

Now the hologram at the Fourier plane is no longer binarized because we just modified the profile at the image plane. Therefore, we will need to apply binarization again. By repeating this cycle, we will be able to reduce the error within the signal window. The binarization error will be “repelled” to the outside of the signal window. One may want to correct the first-order beam only if the edge of the signal window is near or cropping the profile. It is because the negative first-order scattering beam suffer from optical aberrations, and the aberrations can cause the light to “leak” to the outside of the window. Correct first-order beam only may lead to a slower convergence speed but with lower error for the final result.

Note that  $g^{(i)}(\mathbf{x})$  isn't not always a real function. Therefore, we will need to project it into real space first while performing binarization. We have tried both taking the absolute value and the real part of  $g^{(i)}(\mathbf{x})$ , and we did not find any significant difference in the convergence speed. As a result, we use the method of taking the real part because it is less computationally expensive.

To avoid stagnation and lead to a faster convergence, Wyrowski (1989) [24] suggested using an adaptive binarization threshold. At first, we only binarize the value close to 0 and 1, and we change the binarization threshold throughout the iteration.

$$G_b^{(i)} = U_t[G^{(i)}(\mathbf{x})] = \begin{cases} 0 & \text{if } \text{Re}[G^{(i)}(\mathbf{x})] < t \\ 1 & \text{if } \text{Re}[G^{(i)}(\mathbf{x})] > t \\ \text{Re}[G^{(i)}(\mathbf{x})] & \text{otherwise} \end{cases} \quad (2.29)$$

where  $t$  is the threshold. In our algorithm, we sweep the threshold linearly through out the iterations.

$$t = \frac{i}{2N} \tag{2.30}$$

Shown in figure 2.12 is the simulation result using the IFTA with the same target profile used in figure 2.9 and 2.10. We can see that the peak mismatch and crosstalk are significantly reduced. Both of them are less than 1% now. Also, we can see in figure 2.12 (b) the background error becomes less, and we have more artifacts in the area away from the ion positions.

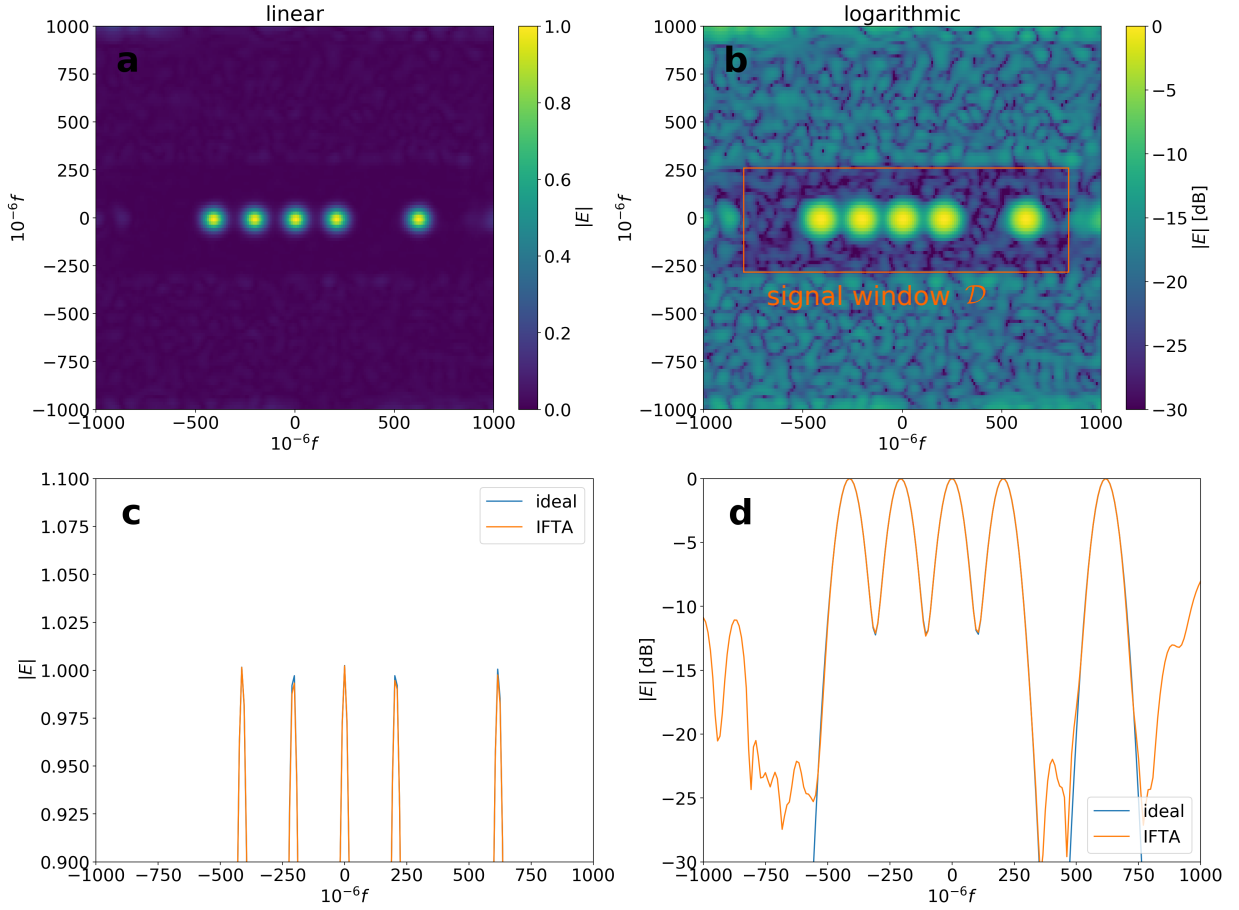


Figure 2.12: Simulation results of beam profile at the image plane with a hologram generated by the iterative Fourier transform algorithm (IFTA) (a) Normalized field amplitude. (b) Normalized field Amplitude in the logarithmic scale. (c) Normalized field amplitude of the cross-section along the ion chain direction. (d) Normalized field amplitude of the cross-section along the ion chain direction in the logarithmic scale. (Simulation condition:  $\lambda = 399\text{nm}$ ,  $f = 728\text{ mm}$ ,  $N = 1500$ ) There is a less than 1% peak mismatch shown in figure c and approximately -25 dBc cross-talk in figure d. The cross-talk reduces by about 10 dB comparing to the results in figure 2.10 It also outperforms the current state-of-the-art trapped ion quantum computer experiment[4].

## 2.7 Chapter Summary

In this chapter, we have introduced a novel algorithm to improve on holographic beam shaping. The holographic beam shaping uses a re-programmable hologram to engineer the beam profile addressed on the ion chain. This method, compared with the existing methods, has the following advantages.

1. With the holographic beam shaping scheme, we have control over not only the amplitude but also the phase of the beam. It is particularly useful if we want to engineer optical-phase-dependent gates.
2. The holographic beam shaping scheme is immune to the imperfection of the optics. The optical aberration inside the system can be compensated by applying a correction phase profile on the hologram.
3. Our setup is a re-programmable setup making it be able to adapt to the unequal spacing between ions in a long-chain configuration.

The device we used as the re-programmable hologram is a digital micro-mirror device (DMD), a device consists of micro-mirrors that can be used as optical switches to give binarized amplitude control (on/off) on the beam profile. To use the DMD as the re-programmable hologram, we need to add the binarization process to the hologram calculation. However, the binarization process makes unwanted artifacts occur at the image plane. We developed a new algorithm that uses iterative Fourier transformation to optimize the beam profile within a region of interest in the image plane. Also, the simulation results show less 1% inaccuracy in amplitude. The simulation shows that our algorithm has about an order of magnitude improvement on accuracy. It also outperforms the current state-of-the-art trapped ion quantum computer experiment[4].

# Chapter 3

## Calibration and Use Cases

### 3.1 Aberration Phase Profile Measurement

One advantage of using holographic beam shaping is the ability to compensate the aberration, making the addressing system immune to optical imperfection. As we have shown in the 2.19, the aberration of the first-order diffraction beam can be cancelled by applying a compensating phase mask while calculating the grating function. To measure the aberration phase profile, one may think of using a Shack-Hartmann wavefront sensor[13]. Although it offers a straightforward method, there are some difficulties we need to deal with. First, the size of micro-lens from a commercially available wavefront sensor is typically larger than  $150\mu\text{m}$ .

In contrast, the micro-mirror on the DMD is only  $10.8\mu\text{m}$ . It limits the resolution of the measurement. Second, there are more beams with diffraction orders, and they may not spatially be separated until it reaches the image plane. Nevertheless, the beam profile at the image plane is small, making it not ideal for a Shack-Hartmann wavefront sensor. Also, ions are inside a vacuum chamber, making it hard to place an external sensor.

In [27], it has been demonstrated that the aberration phase profile can be measured by opening two small patches of gratings on the DMD and measuring the interference pattern of the beams reflecting from the two patches. The setup is illustrated in figure 3.1. The two patches are separated by a distance  $d$ . Since the patches we opened are small, the beam profile at image plane after the optical Fourier transformation can be approximated as a plane wave. We denoted them as  $E_1(\mathbf{x})$  and  $E_2(\mathbf{x})$  with optical phases  $\phi_1$  and  $\phi_2$

respectively.

$$E_1(\mathbf{x}) = A_1 e^{i(\mathbf{k}_1 \cdot \mathbf{x} + \phi_1)} \quad (3.1)$$

$$E_2(\mathbf{x}) = A_2 e^{i(\mathbf{k}_2 \cdot \mathbf{x} + \phi_2)} \quad (3.2)$$

The total intensity contributes from both beams shows an interference pattern. The spatial phase of the interference fringes corresponds to the phase difference of the two patches.

$$I_{tot}(\mathbf{x}) = |E_1(\mathbf{x}) + E_2(\mathbf{x})|^2 \quad (3.3)$$

$$= |A_1|^2 + |A_2|^2 + 2A_1A_2 \cos((\mathbf{k}_1 - \mathbf{k}_2) \cdot \mathbf{x} + \phi_1 - \phi_2) \quad (3.4)$$

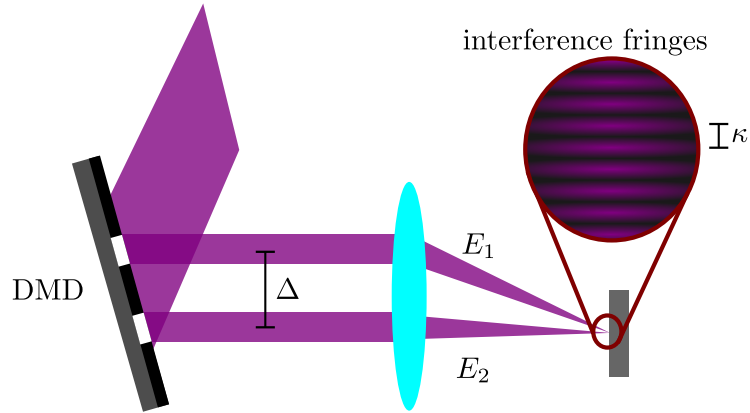


Figure 3.1: Illustration of the setup for aberration phase profile characterization.

To retrieve the spatial phase from the interference fringes, Zupancic (2013)[27] uses a pinhole along with a photodiode to measure the intensity at the first order origin and scan the fringes by varying the phase of the grating patch. In our experiment, we use a camera to image the interference fringes instead. One of the camera images of the fringes is shown in figure 3.2.

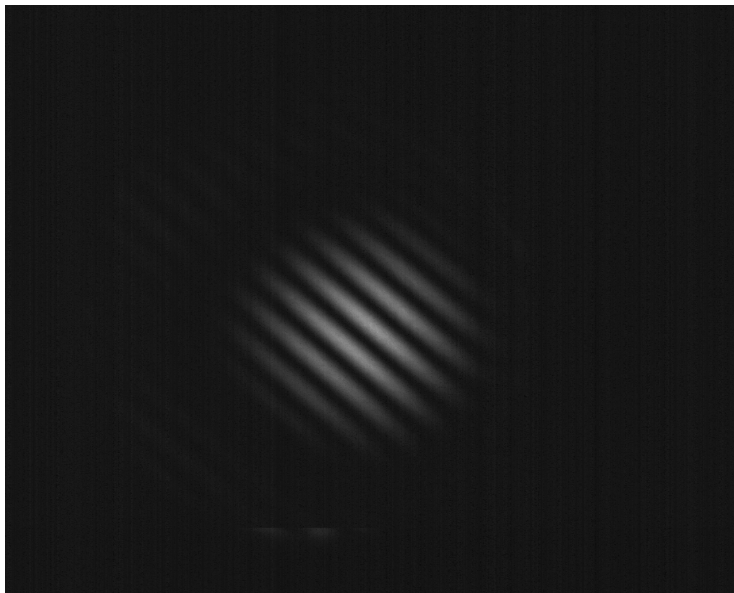


Figure 3.2: A camera image of the interference pattern. camera model: BFLY-PGE-05S2M-CS, Fourier lens focal length = 500 mm

To retrieve the spatial phase of the fringe, we first sum the image over the axis which is perpendicular to the separation direction of two patches(perpendicular to  $\mathbf{k}_1 - \mathbf{k}_2$ ) and get the 1D profile  $f(x)$  after summation. The spatial phase of the interference fringes  $\psi = \phi_1 - \phi_2$  can be extracted by taking the correlation<sup>1</sup> of  $f(x)$  and a test signal  $e^{i\kappa(x-x_0)}$ .

$$C = \text{corr}(e^{i\kappa(x-x_0)}, f(x)) \quad (3.5)$$

in which  $\kappa$  is the spatial frequency of the interference fringe. The spatial frequency depends on the separation of the two patches. Similar to the equation 2.8 and 2.9, we have:

$$\kappa = |\mathbf{k}_1 - \mathbf{k}_2| = \frac{2\pi}{\lambda f} \Delta \quad (3.6)$$

where  $\Delta$  is the separation of two patches. To reconstruct the 2D phase profile, we need the phase difference profile in two directions. By making the two patches separated along x and y axis, we have the phase difference profile  $\Psi_x(x, y)$  and  $\Psi_y(x, y)$ .

$$\Psi_x(x, y) = \Phi(x + \Delta, y) - \Phi(x, y) \quad (3.7)$$

$$\Psi_y(x, y) = \Phi(x, y + \Delta) - \Phi(x, y) \quad (3.8)$$

<sup>1</sup><https://docs.scipy.org/doc/numpy/reference/generated/numpy.correlate.html>

We then fit the phase profile  $\Phi(x, y)$  with a series of Zernike polynomials. The result is shown in figure 3.3. We can see before aberration compensation the aberration is about across the aperture is five waves. To examine the aberration compensation, we perform the experiment again. However, we subtract the aberration phase while making the grating patch this time. As we can see in figure 3.4, the wavefront uniformity has been greatly improved. The aberration across the aperture is less than 0.1 waves, which is a 50 times improvement.

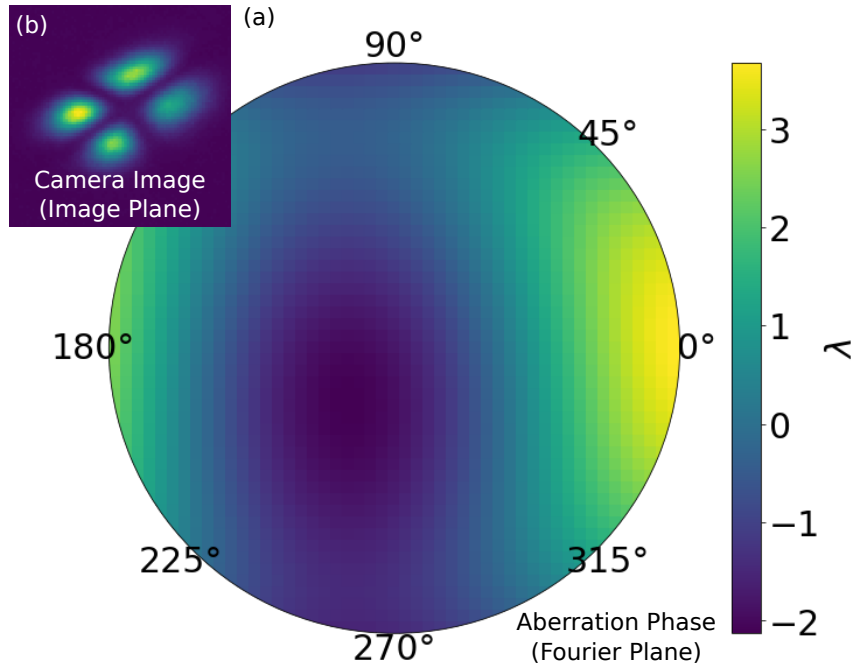


Figure 3.3: Phase map of the aberration phase before aberration compensation. (a) The aberration phase profile at the Fourier image. The aberration is about five waves across the aperture. The profile is obtained by fitting a series of Zernike polynomials up to fourth-order (The constant phase term is excluded.). (b) Camera image of Gaussian TEM<sub>11</sub> mode created with holograph beam shaping without aberration compensation. The non-uniform illumination results from incomplete power calibration. The wavelength we used in the experiment is 399 nm, and the radius of the aperture is 6 mm.



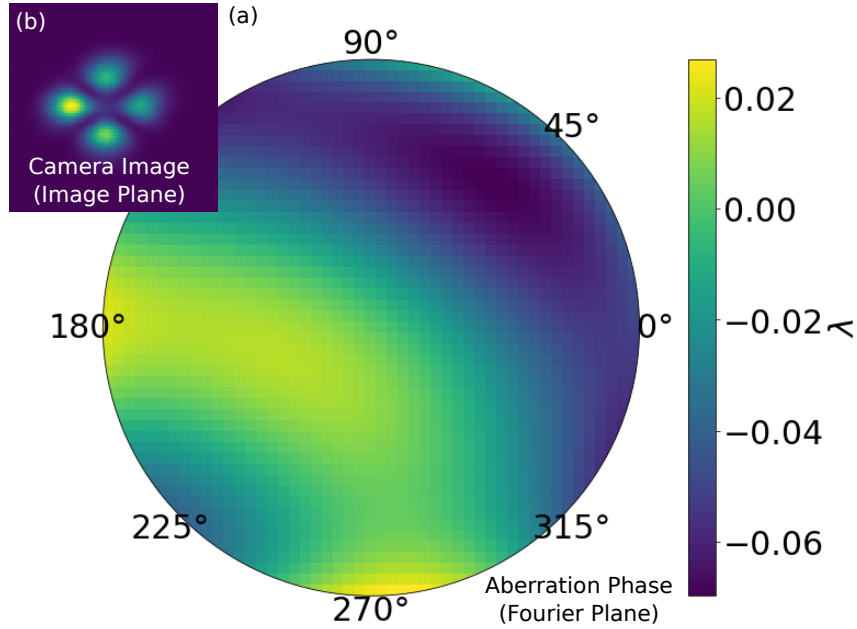


Figure 3.4: Phase map of the aberration phase after aberration compensation. (a) The aberration phase profile at the Fourier image. The aberration is less than 0.1 waves across the aperture. It is a 50 times improvement than the aberration before aberration compensation shown in figure 3.3. (b) Camera image of Gaussian  $TEM_{11}$  mode created with holograph beam shaping with aberration compensation. The non-uniform illumination results from incomplete power calibration. The profile is obtained by fitting a series of Zernike polynomials up to fourth-order (The constant phase term is excluded.). The wavelength we used in the experiment is 399 nm, and the aperture radius is 6 mm.

## 3.2 Aberration Calibration with An Ion

In section 3.1, we have discussed how to measure the aberration phase profile with a camera placed in the image plane and demonstrated that it could be compensated. However, when we use it as an addressing apparatus for ions, the final image plan is inside the vacuum chamber, which may make it unreachable with conventional sensors. Hence, we proposed the idea of using a trapped ion as the sensor. To do so, we need the ability to measure the intensity of the light at the ion position and a way to scan the interference fringes. For an off-resonance beam, the power measurement can be done by measuring the differential AC Stark shift between two-qubit states with standard techniques such as

Ramsey spectroscopy. As for the resonance beam, we can measure the power from the fluorescence of the ion. To scan the interference fringes, we can use either of the two methods:

1. Changing the DC voltages on the electrodes to move the ion across the trap.
2. Deploy a piezo-controlled mirror on the Fourier plane. The tilt of the mirror corresponds to the transnational displacement on the image plane.

### 3.3 Maximizing Diffraction Efficiency

The mirror array on the DMD itself forms a grating that that can diffract the light into not just one of the two directions. The interference pattern from the micro-mirror array grating comes with an envelope which is defined by the diffraction pattern from a single micro-mirror. Note that the grating we are talking here is not the grating profile we have discussed in the equation 2.19, the grating here comes from the periodic structure of the micro-mirror array. As figure 3.5 shows, each diffracted beam from the micro-mirror grating contains beams of the three diffraction orders from the hologram grating.

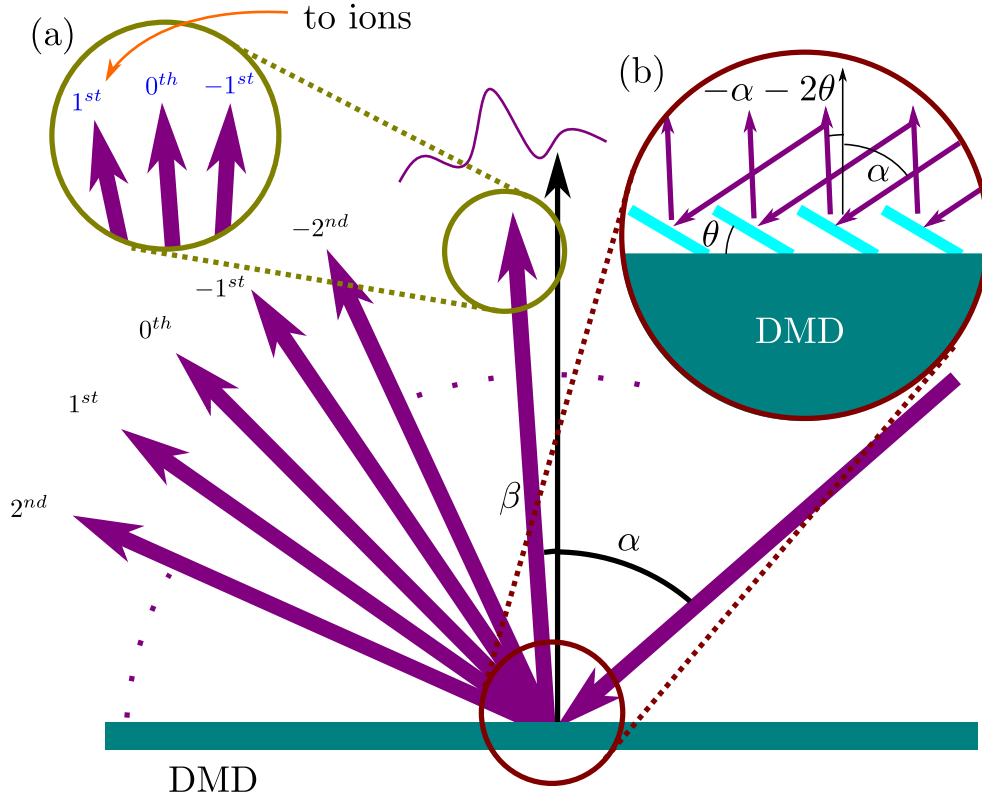


Figure 3.5: Illustration of multiple diffraction beams from the micro-mirror array grating. (a) Each diffraction beam from the micro-mirror array grating has three diffraction order beams from the hologram grating. (b) The law of reflection of micro-mirrors.

To maximize the diffraction efficiency of the DMD, we want the envelope to overlap with the diffraction beam we are interested in, so we can channel more power to the target beam profile. The center of the diffraction envelope satisfies the law of reflection of a single mirror.

$$\beta = -\alpha - 2\theta \quad (3.9)$$

where  $\alpha$  and  $\beta$  are the incident angle respectively, and  $\theta$  is the tilt angle of the micro-mirror which is 12 degrees in our DMD. As for the micro-mirror grating, it follows the grating equation.

$$\sin \alpha + \sin \beta = \frac{\sqrt{2}n\lambda}{d} \quad (3.10)$$

Here,  $n$  states the diffraction order of the mirror-mirror grating, and  $d$  is the edge length of a micro-mirror. The  $\sqrt{2}$  factor comes from the fact that the micro-mirror is flipped along

the diagonal axis. (Figure 2.4). Combine equation 3.9 and equation 3.10, we get:

$$\sin \alpha + \sin (-\alpha - 2\theta) = \frac{\sqrt{2}n\lambda}{d} \quad (3.11)$$

We solve the equation numerically, and the results are shown in figure 3.6 where the zero-crossing points are. There are multiple solutions depends on the diffraction order we choose. In our experiment, we use the -8th diffraction order because the reflection angle  $\beta$  is close to 0 degree and it has less distortion from tilt.

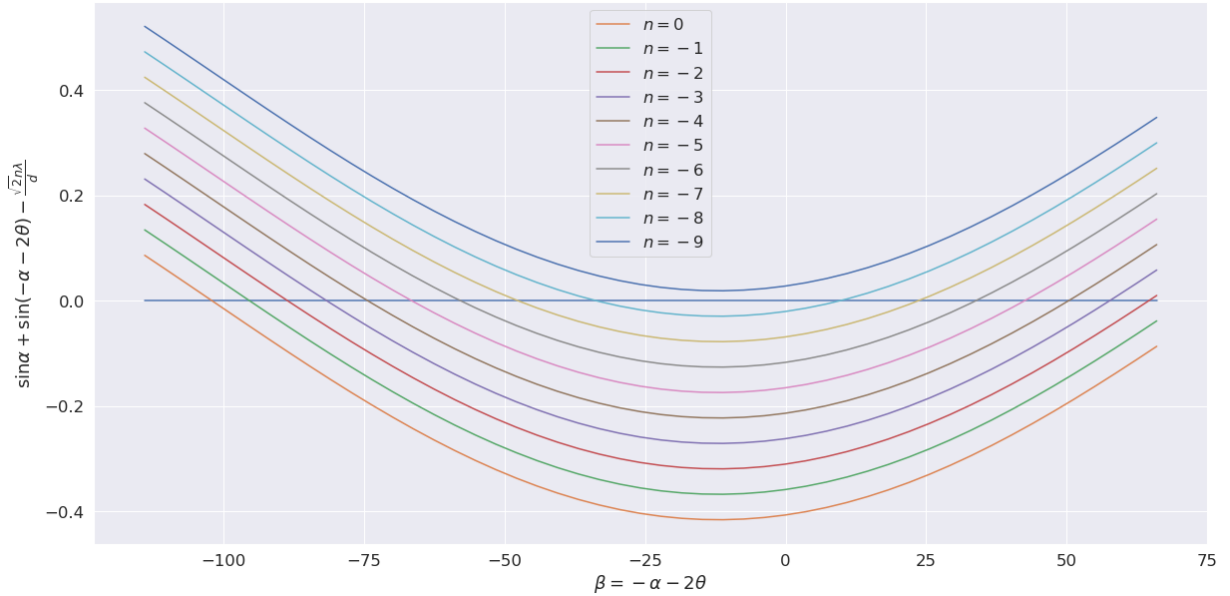


Figure 3.6: Solutions for equation 3.11 with different diffraction order. The solutions indicates the condition of maximized diffraction efficiency. The solutions are at the zero crossing points. The solutions exist between zeroth order to negative eighth order. For each order, there will be two solutions. Condition:  $d = 10.8 \text{ um}$ ,  $\lambda = 369\text{nm}$

### 3.4 Use case: Linear Gradient Intensity

An application of individual addressing is arbitrary single-qubit phase gates. We can use off-resonance beams to induce different amounts of phase shift to different qubits with the AC Stark shift effect.

To understand the AC Stark shift, first, we consider a two-level system as figure 3.7 shows. The energy separation between ground state  $|g\rangle$  and excited state  $|e\rangle$  is  $\omega_e$ . (letting  $\hbar = 1$ ) The two states are off-resonantly coupled with a laser with frequency  $\omega$  and Rabi frequency  $\Omega$ . The laser is detuned  $\Delta$  from the transition. We can write the Hamiltonian of the system as the following equation.

$$H = \frac{\omega_e}{2} |e\rangle \langle e| - \frac{\omega_g}{2} |g\rangle \langle g| + \frac{\Omega}{2} (|e\rangle \langle g|)(e^{i\omega t} + e^{-i\omega t}) + h.c. \quad (3.12)$$

We can bring the Hamiltonian to the laser rotating frame.

$$H_{rot} = e^{iH_0 t} (H - H_0) e^{-iH_0 t} \quad (3.13)$$

$$= -\frac{\Delta}{2} |e\rangle \langle e| + \frac{\Delta}{2} |g\rangle \langle g| + \frac{\Omega}{2} (|e\rangle \langle g|)(e^{i2\omega t} + 1) + h.c. \quad (3.14)$$

where

$$H_0 = \frac{\omega}{2} |e\rangle \langle e| - \frac{\omega}{2} |g\rangle \langle g| \quad (3.15)$$

. We can ignore the fast rotating term  $e^{i2\omega t}$  in equation 3.14 with the rotating wave approximation (RWA).

$$H_{rot} \approx -\frac{\Delta}{2} |e\rangle \langle e| + \frac{\Delta}{2} |g\rangle \langle g| + \frac{\Omega}{2} (|e\rangle \langle g|) + h.c. \quad (3.16)$$

As we can see now, the Hamiltonian is time independent. By diagonalizing the Hamiltonian, we can obtain the eigen states and their energy. With the assumption that  $\Delta \gg \Omega$ , we have the new eigen energies become:

$$E_{rot} = \pm \sqrt{\frac{\Delta^2}{4} + \frac{\Omega^2}{4}} \quad (3.17)$$

$$\approx \pm \left( \frac{1}{2} \Delta + \frac{\Omega^2}{4\Delta} \right) \quad (3.18)$$

Comparing with equation 3.16, we can find that  $\frac{1}{2} \Delta + \frac{\Omega^2}{4\Delta}$  corresponds to the energy of the shifted ground state, and the other one corresponds to the energy of the shifted excited state. We can find the energy shift is proportional to the square of  $\Omega$ .

$$\delta E_g = + \frac{\Omega^2}{4\Delta} \quad (3.19)$$

$$\delta E_e = - \frac{\Omega^2}{4\Delta} \quad (3.20)$$

For a multi-level system, the total AC Stark shift are the sum over the contributions from all the excited states.

$$\delta E_g = \sum_i \frac{\Omega_i^2}{4\Delta_i} = \frac{g_0^2}{4} \sum_i \frac{B_i^2}{\Delta_i} \quad (3.21)$$

where  $B$  is the branching ration and  $g_0^2 = \Gamma^2 \frac{I_{laser}}{2I_{sat}}$ .  $\Gamma$  is the nature linewidth of the transition.  $I_{laser}$  is the intensity of the laser, and  $I_{sat}$  is the saturation intensity.

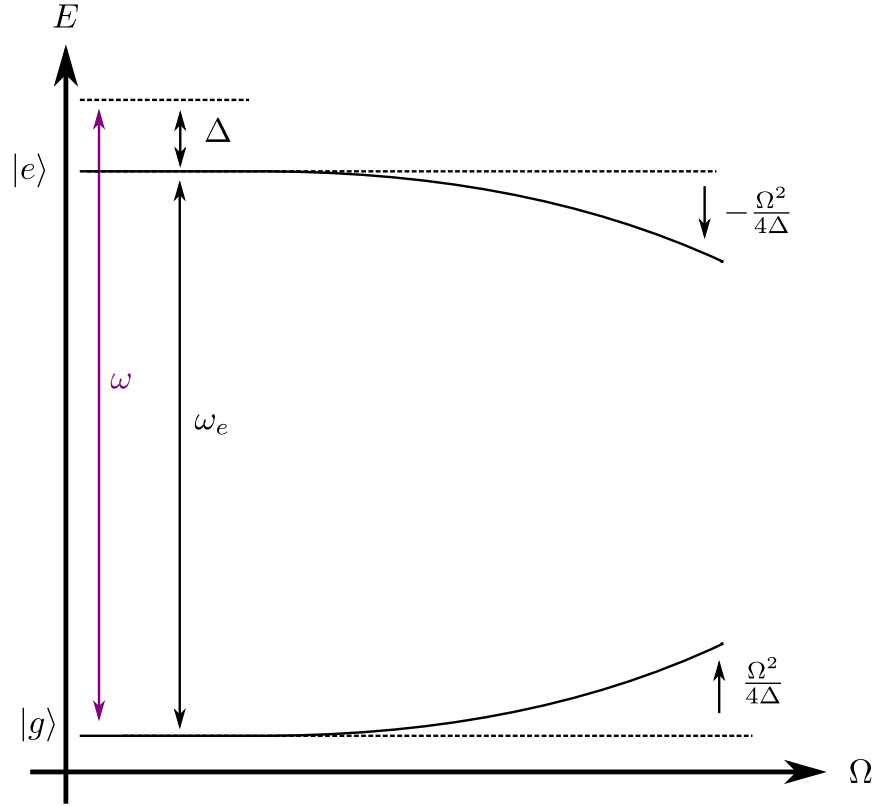


Figure 3.7: AC Stark shift in a two-level system.

As figure 3.8 shows, for  $^{171}\text{Yb}^+$ , most of the contributions are from  $^2P_{1/2}$  and  $^2P_{3/2}$  excited states. We can calculate the AC Stark Shift of the two-qubit states. (The branching ratio calculations are in appendix A.) For the beam with arbitrary polarization, the energy

shifts of the two-qubit states are:

$$\delta E_0 = \frac{g_0^2}{12} \left( \frac{1}{\Delta} - \frac{2}{\omega_F - \Delta} \right) \quad (3.22)$$

$$\delta E_1 = \frac{g_0^2}{12} \left( \frac{1}{\Delta + \omega_{HF}} - \frac{2}{\omega_F - \Delta - \omega_{HF}} \right) \quad (3.23)$$

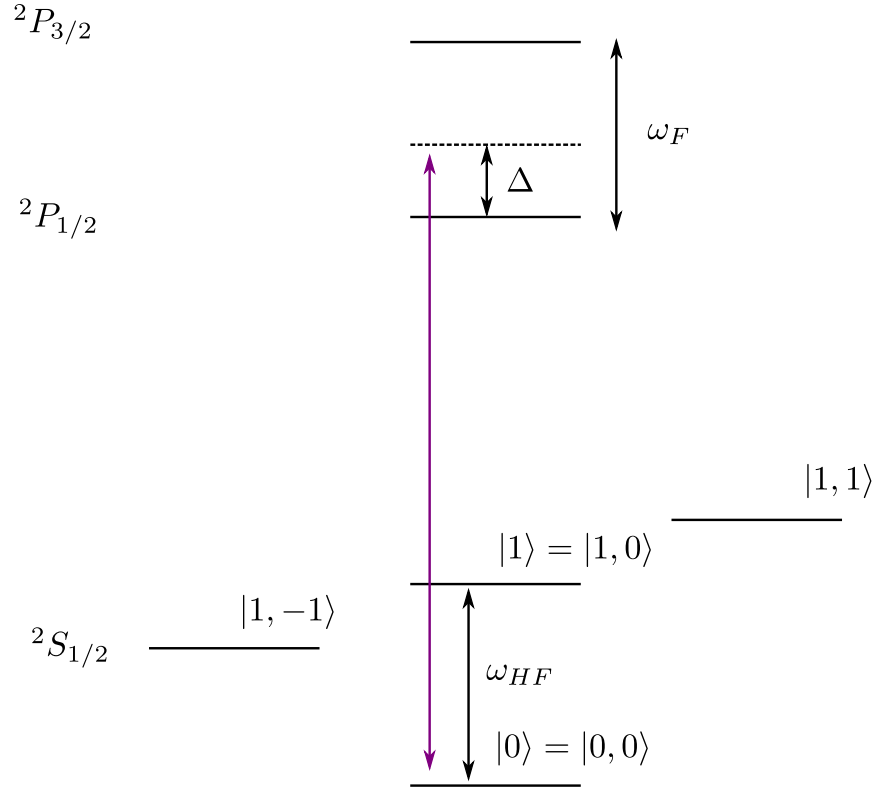


Figure 3.8: AC Stark shift of  $^{171}\text{Yb}^+$ .

We can find difference energy shifts from the two-qubit states contributes to a non-zero differential AC Stark shift.

$$\delta\omega_{qubit} = \delta E_0 - \delta E_1 \quad (3.24)$$

which is proportional to the intensity of the laser.

$$\omega_{qubit} \propto g_0^2 \propto I_{laser} \quad (3.25)$$

Therefore, we can have addressing patterns that have different intensity on different ions. With the same amount of the operation time, the phase shift is proportional the local intensities.

As an example, figure 3.9 shows a linear intensity gradient intensity profile we created with the holographic beam shaping. This particular example can be used in our theory proposal[15] in which global Mølmer-Sørensen gates and arbitrary single-qubit phase gates are used to simulate 2D lattices in a hybrid digital-analog way.

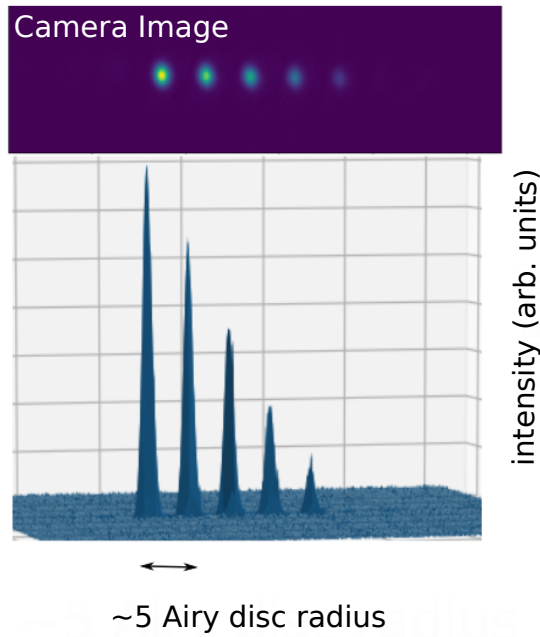


Figure 3.9: A linear gradient intensity pattern created by holographic beam shaping.  $\lambda = 399$  nm. It can be used to create site-dependent phase shifts that can be used in the quantum simulation experiment from Rajabi et al. (2019)[15]

### 3.5 Chapter Summary

In this chapter, we discussed some important considerations for implementing the holographic beam shaping scheme that has been proposed in chapter 2.



1. Maximizing Efficiency: The micro-mirror array itself acts as a grating that creates multiple diffracted beams. Each diffraction order contains the negative first, zeroth, and first diffraction order from the hologram grating. The diffracted angles of the beams follow the grating equation. On top of the diffraction patterns from the grating, there is an envelope which corresponds to the diffraction pattern of a single micro-mirror. The center of the envelope where it also has the maximum value follows the law of reflection. To channel as much as energy possible to the beam with the desired diffraction order, one needs to find a proper input angle such that the center of the envelope aligns with the beam. The angle can be found by solving the grating equation and the law of reflection at the same time.
2. Aberration Compensation: In the previous chapter, we have shown the optical aberration can be compensated by applying a correction phase profile while calculating holograms. To find the correction phase profile, we need to characterize the optical aberration in the system. We showed that the aberration phase could be measured by opening two patches on the DMD. The beams from the two patches overlap at the image forming interference fringes. The spatial phase of the interference fringes corresponds to the phase difference between the two patches. By shifting the patches across the DMD, we can reconstruct the aberration phase profile. We also discussed the plan to use a single ion as a detector to measure the interference fringes at the final image plane when we integrate the system to an ion trap in the future.

Along with the experimental considerations, we also show a use case of holographic beam shaping. In this use case, we engineer a linear gradient intensity profile that can be converted to phase shifts on the ions through the AC Stark shift. It can be used in our recent theoretical proposal[15] which simulates the dynamics of 2D lattices in a linear chain of ions.

# Chapter 4

## Holographic Addressing with Multiple Frequency Channels

As we discussed in section 1.2, it is required to have the individual addressing ability of beams with different frequencies to have full control over the spin-spin interaction graph. As the schematic in figure 4.1 show, an AOM combining with a cylindrical convex lens is used to split the light onto different zones of the DMD. These zones correspond to different RF input frequencies. They act as different frequency channels. Each channel has its hologram for controlling the amplitudes and phases of the beams addressed on individual ions.

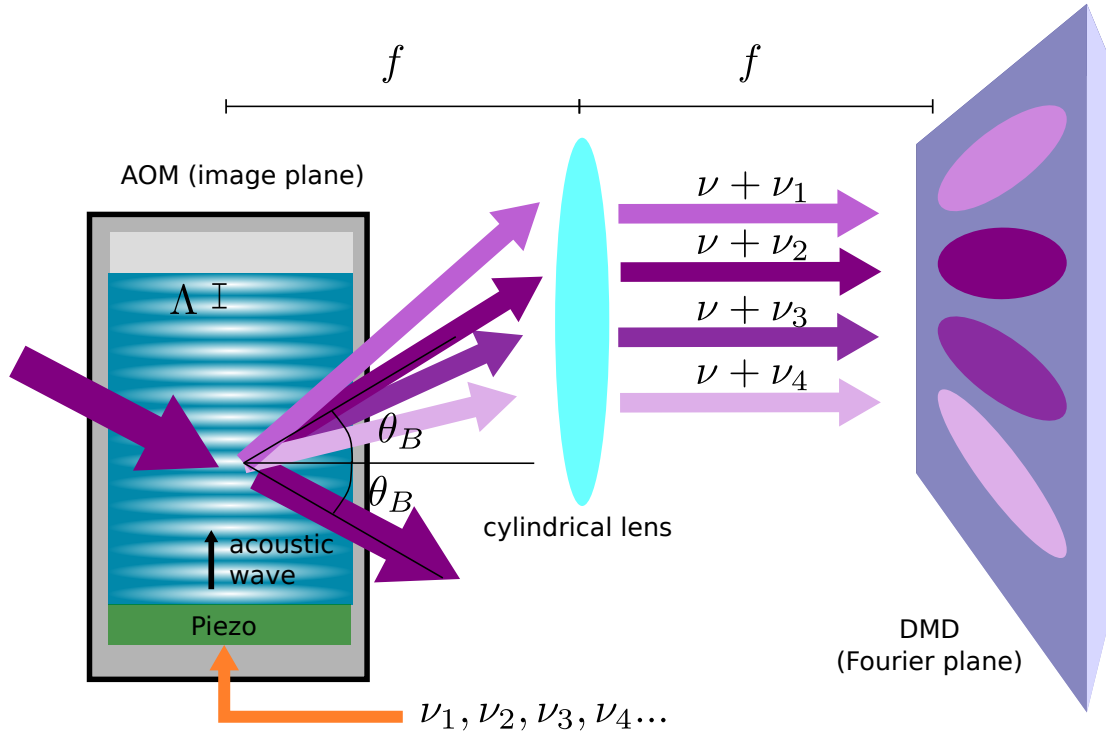


Figure 4.1: Illustration of generating multiple beams with an AOM for different frequency channels.

There are two types of AOM, Raman-Nath type and Bragg type. The AOM we used is a Bragg type modulator. The diffraction angle satisfies the Bragg condition as the figure shows. For the first-order diffraction beam, the Bragg angle is

$$\theta_B = \sin^{-1} \frac{\lambda}{2\Lambda} \quad (4.1)$$

where  $\lambda$  is the wavelength of the incoming beam and  $\Lambda$  is the wavelength of the acoustic wave in the crystal of the AOM. With the Bragg angle  $\theta_B$ , the wavevector  $\mathbf{k}_\nu$  that added to the diffracted beam is

$$k_\nu = 2k_0 \sin \theta_B = \frac{k_0 \lambda}{\Lambda} = 2\pi \frac{1}{\Lambda} \quad (4.2)$$

in which  $k_0$  is the wavevector of the incident beam. The wavelength of the acoustic wave depends on the speed of sound in the crystal  $v$  and the modulation frequency  $\nu$ .

$$k_\nu = 2\pi \frac{\nu}{v} \quad (4.3)$$

The wavevector  $\mathbf{k}_\nu$  is along the propagation direction of the acoustic wave which is almost perpendicular to the propagation direction of the beam. The frequency of the diffracted beam also depends on the modulation RF frequency. For the first-order diffraction beam, the modulation frequency is added to the frequency of the beam. As a result, by applying multiple-tone RF to the AOM, we can split a beam into several beams, and each of them has a different frequency detuning.

$$\Delta k_\nu = 2\pi \frac{\Delta\nu}{v} \quad (4.4)$$

To determine what the minimum frequency splitting is required for avoiding the crosstalk between the adjacent frequency channels, we will need to know the beam waist of the diffracted beam. Consider an incident Gaussian beam with waist radius  $w_0$ , its Fourier transform shows.

$$\mathcal{F}\left[e^{-\frac{x^2}{w_0^2}}\right] \propto e^{-\frac{k^2}{(2/w_0)^2}} = e^{-\frac{k^2}{k_w^2}} \quad (4.5)$$

It reveals that the waist radius of the Gaussian beam in Fourier space  $k_w$  is inverse proportional to the beam waist.

$$k_w = \frac{2}{w_0} \quad (4.6)$$

Assume the minimum separation to be  $\gamma$  times of the waist radius.

$$\Delta k_\nu = \gamma k_w \quad (4.7)$$

We can find the required frequency difference.

$$\Delta\nu = \gamma \frac{v}{\pi w_0} \quad (4.8)$$

For a given  $\gamma$ , it only depends on the dimension of the incident beam and the material property of the crystal. The materials commonly used as the crystal in the AOM are tellurium dioxide, fused silica, germanium, and quartz. However, not all of them have good transmission efficiency in the UV spectrum. As a result, we use an AOM from Intraaction Inc. which use fused silica. The speed of sound in fused silica is about 5968 m/s [23]. In our experiment, we choose to have at least a 2MHz separation between frequency channels.

## 4.1 Frequency Channels Preparation

In the previous section, we described the method of generating multiple beams with different frequencies illuminating different zones of the DMD. One thing we have to be aware

of is that it implies the Fourier plane is divided, and each beam only takes a part of the Fourier plane in order not to overlap with other beams. As a consequence, this limits the ability to generate diffraction-limited profiles at the image plane. The size of the profile each beam can generate is roughly inverse proportionally to the size of the occupied area in the Fourier plane. To get around with this problem, we introduce cylindrical lenses into the system. We shape the beams to make them have elliptical shapes on the DMD. The beams are separated along the short axis and expand across the Fourier plane along the long axis. The long axis of the beam on the DMD corresponds to the axial direction of the ion chain, and the shot axis corresponds to the radial direction. Although generating diffraction-limited spots with multiple frequencies is still unavailable with this setup due to the fundamental limitation of the segmented Fourier plane, we can achieve diffraction-limited addressing along the axial direction by increasing the beam waist at the Fourier plane along this direction.

Figure 4.2 is the schematic of the optics we built to prepare these elliptical beams. (The picture of the setup is shown in figure 4.2) We first expand the beam in the horizontal direction before the AOM with a telescope which is made of cylindrical lenses. The AOM splits the light into multiple beams. The neighbouring beams have a 2 MHz difference in frequency.

After the AOM, the beam will pass through a cylindrical lens which serves the same purpose as the lens in figure 4.1. The center of the AOM is placed at the focal plane of the cylindrical lens, making the angular separation of beams converted to the transnational separation. The only difference is we have a cylindrical telescope and a telescope to shape the beams to the proper size before them land the DMD. As figure 4.2 (a) shows, the beams are elliptical on the DMD. The long axis is along the vertical direction. It is also noteworthy that we put the AOM at another image plane relative to the DMD, so the beam of different frequencies will be combined at the camera position (image plane) without the need to add extra phase gradient on the hologram.

In summary, we segmented the Fourier plane into several areas and illuminated each area with a beam with different frequency. They are acting as different frequency channels. Each of the channels has its hologram for amplitude modulation and phase control. Although the Fourier plane is segmented, we still have the beam to span across the Fourier plane along the ion chain direction. It enables us to have diffraction-limited addressing in this direction.

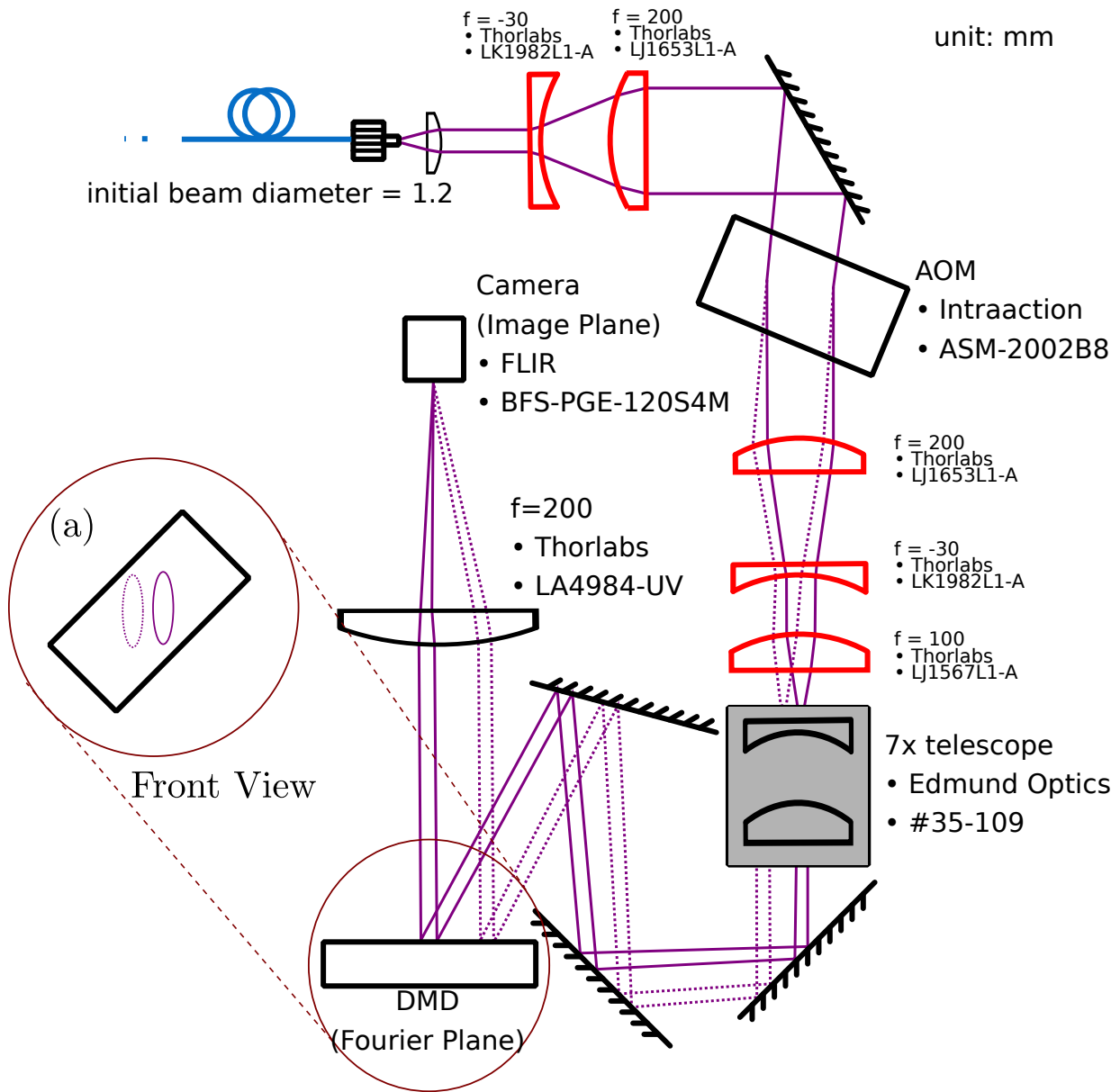


Figure 4.2: Schematic of the optical setup for the multi-frequency addressing scheme. The cylindrical optics which shapes the beams in horizontal directions uses the red colour in the schematic.

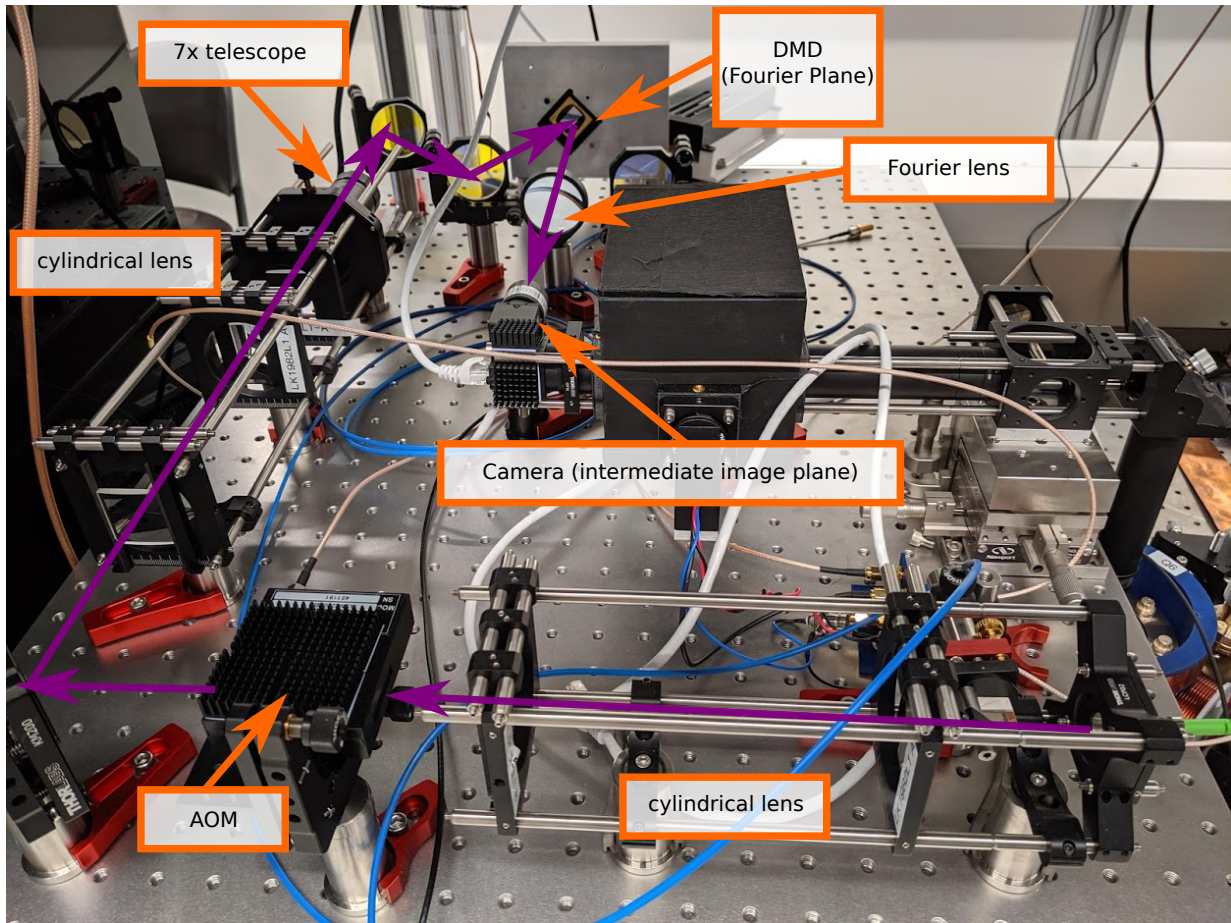


Figure 4.3: Picture of the optical setup for the multi-frequency addressing scheme. The purple arrows indicates the beam path. The schematic of the setup is shown in figure 4.2

## 4.2 Experiment Results

Shown in figure 4.4 is the intensity profile of a frequency channel on the DMD. Note that the DMD is rotated at 45 degrees, so the long axis of the beam is along the vertical direction. The  $1/e^2$  width of the beam in the horizontal direction (short axis) is around  $100\ \mu\text{m}$  to  $200\ \mu\text{m}$ . The intensity profile is by turning on patches of mirrors and measure the intensity of the light from the reflection.

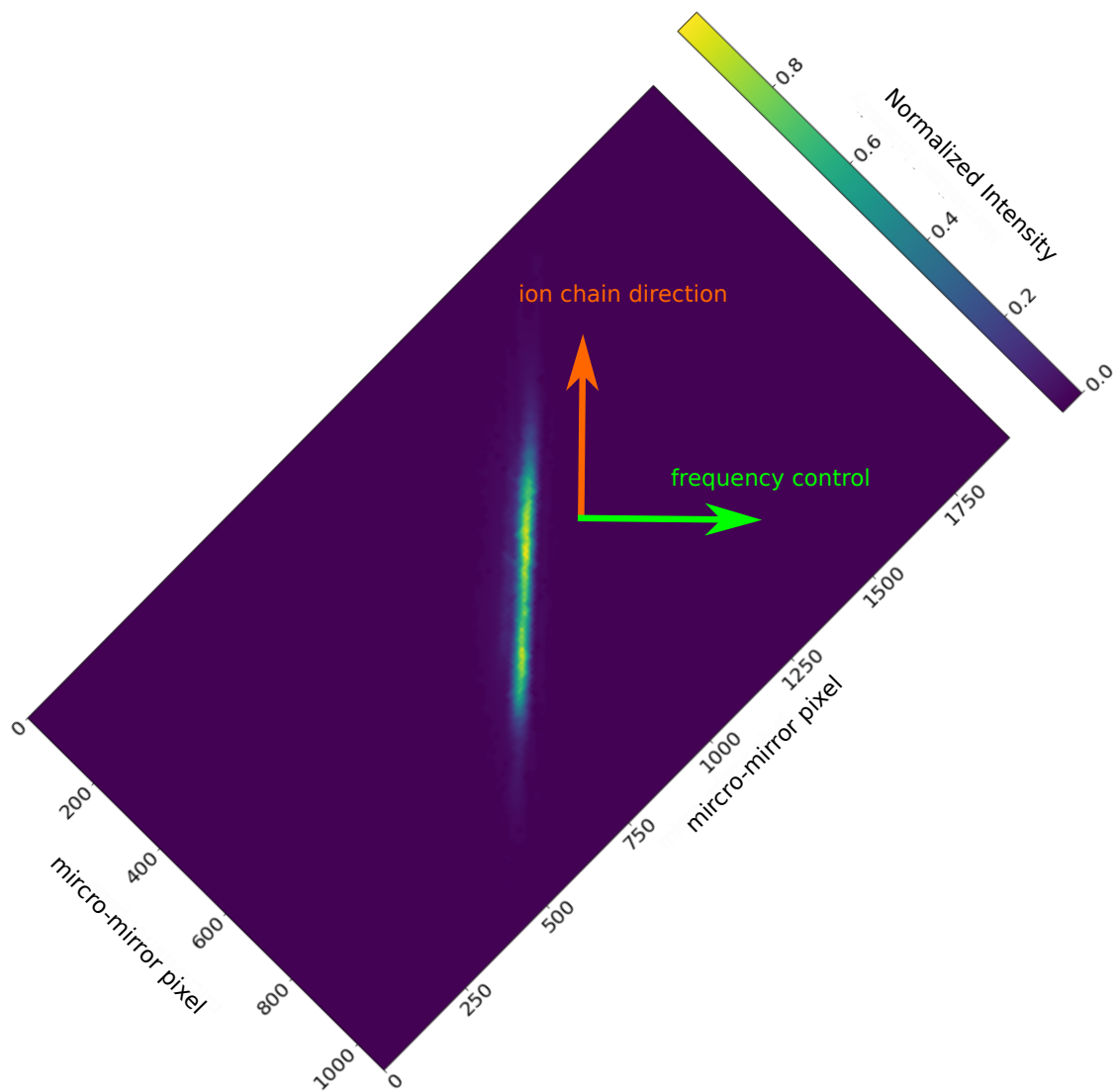


Figure 4.4: Intensity profile of the beam of a frequency channel on the DMD. The size of a micro-mirror pixel is  $10.8 \mu\text{m} \times 10.8 \mu\text{m}$ .

To measure the aberration phase, we use the techniques described in section 3.1. The difference is that we fixed one of the patches at the center of the aperture, and scan



the other patch along the long axis direction. The results are fitted with a third-order polynomial and are shown in figure 4.5.

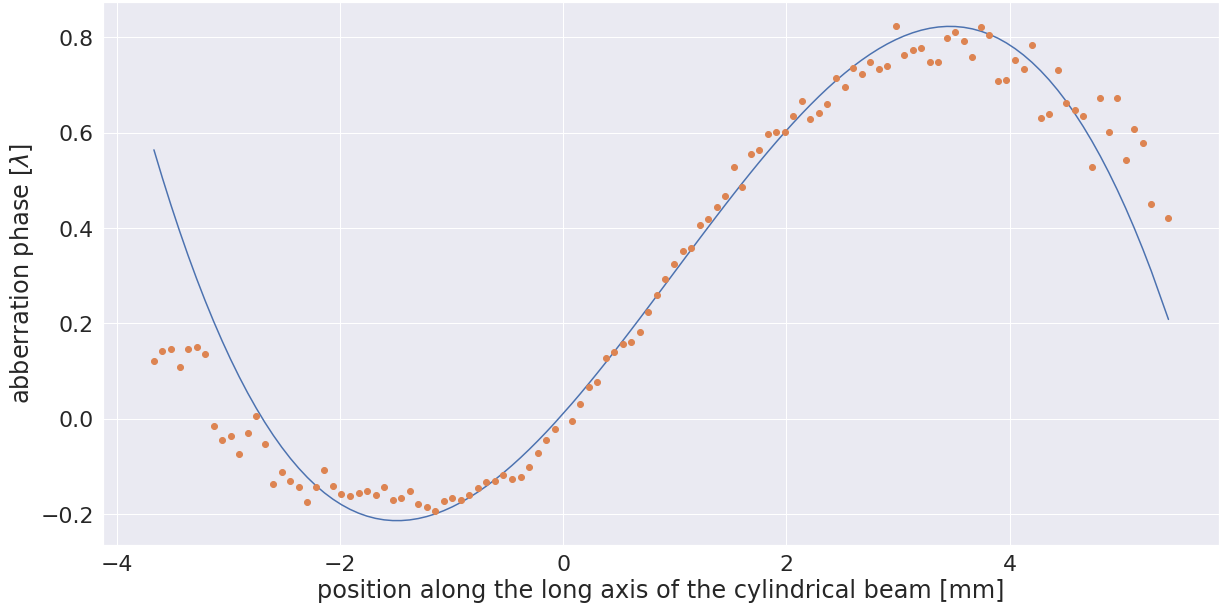


Figure 4.5: Aberration phase profile of the beam along the long axis of a frequency channel on the DMD. The profile is fitted to a third-order polynomial.

To demonstrate we can use the scheme for ion addressing, we create a profile that can be used to address all ions except the third one for a four-ion system. Figure 4.6 shows the intensity profile at the image plan taken by a camera. The binarization method we use is IFTA with the signal window spanning from about 350 to 700 camera pixel in the vertical direction and 450 to 550 camera pixel in the horizontal direction. Note that the ion chain direction corresponds to the vertical direction. Note that the long axis of a cylindrical beam at the Fourier plane will become short axis in the image plane.

The crosstalk is around -30 dB in intensity which corresponds to about -15 dB in field amplitude. Comparing to our simulation results which show having crosstalk around -20 dB, we think the experiment can be improved by further optimizing the aberration phase profile measurements with a full 2D scan.

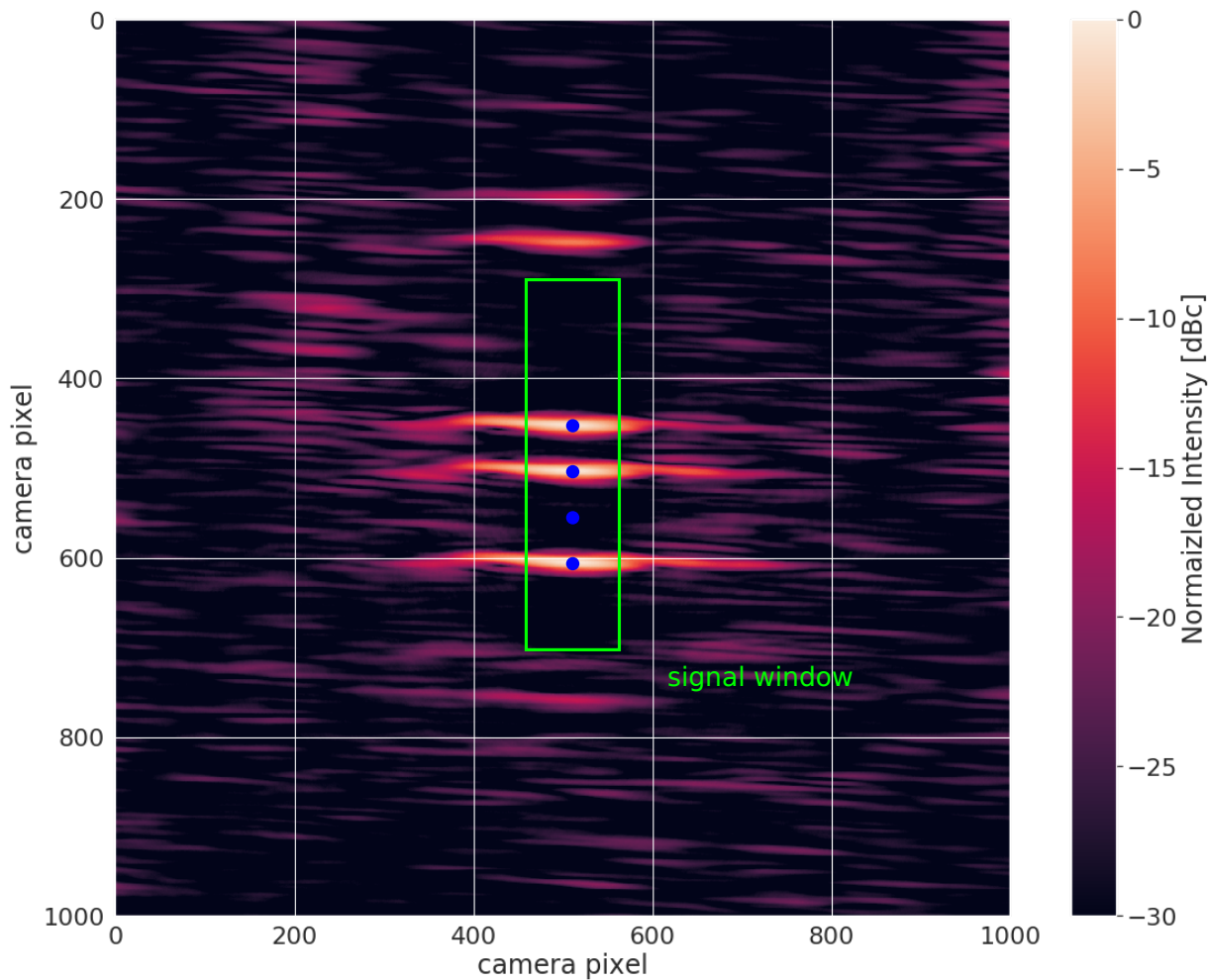


Figure 4.6: The camera image of an addressing profile shaped from one frequency channel. The green box shows the boundary of the signal window, and the blue dots indicate the position of addressing targets. The experimental result shows it has less than -30db dBc crosstalk in intensity of light. Binarization method: IFTA, camera pixel size:  $1.85 \mu\text{m} \times 1.85 \mu\text{m}$

### 4.3 Chapter Summary

To have full control over spin-spin interaction between ions, we need to have frequency control over the laser beams. We proposed and demonstrated a scheme that adding fre-

quency control to the holographic beam shaping scheme. The frequency is implemented with an AOM. The AOM splits the light onto multiple zones on the DMD, and the light on each zone has a different frequency which depends on the RF frequency fed to the AOM. Each zone acts as a frequency channel, and a hologram is displayed on it for modulating the beam of the frequency channel.

In this chapter, we discussed the criteria to separate the beams between adjacent channels for illuminating different zones of the DMD. We found it depends on the size of the input beam for the AOM and the material used as the crystal in the AOM. We built an optics setup for preparing frequency channels. Several pieces of cylindrical optics are used in setup, making the beams illuminated on the DMD has an elliptical shape. It makes the beams still span across the Fourier plane to achieve diffraction-limited addressing while segmenting the Fourier plane for frequency control. Finally, we demonstrated making aberration-corrected addressing beams created from a single frequency channel. The experimental results show a -30dB crosstalk in intensity.

# Chapter 5

## Summary and Outlook

In summary, we have developed a binarization algorithm that is optimized for creating addressing profiles in the trapped ion system. The algorithm shows an order of magnitude improvement in increasing the accuracy. We also experimentally demonstrated aberration compensation and holographic beam shaping experimentally in the ultra-violet wavelength suitable for  $^{171}\text{Yb}^+$ . The UV wavelength is more sensitive to the environment perturbation than the visible or IR due to its short wavelength. We experimentally demonstrate that the wavefront flatness could be corrected to less than 0.15 waves across a Fourier plane aperture of 6mm diameter.

Also, we developed a scheme for adding frequency control to the holographic beam shaping addressing system. By using an AOM to separate the light and illuminating different zones on the DMD, we can simultaneously address ions with beams having different frequencies. It can be handy for engineering Ising spin-spin interaction with the Mølmer-Sørensen scheme[10].

For future integrating the holographic beam shaping techniques to the ion trap we have, we plan to use a single ion as a sensor for calibrating the aberration from optics including the microscope objective since the final image plane locates inside the Vacuum chamber that is not reachable with a conventional device. More discussions on the plan are in section 3.2.

Another challenge for integrating the holographic beam shaping system to an ion trap is the use of picosecond pulsed laser. It is commonly to pulsed laser for the operation of two-photon Raman transition in order to cover the hyperfine splitting in electronic states of nonzero nuclear spin ions [4]. The use of picosecond pulsed laser simplifies the need for preparing another mode-locked laser. However, the broadened frequency due to the finite

pulse width can cause the broadening of the beam profile at the image plane. It is because the scaling between wavevectors at the Fourier plane and distances at the image plane is wavelength-dependent. The problem can be mitigated by reducing the micro-mirror array diffraction order of the beam shown in figure 3.5. The detailed analysis can be found in appendix B.

In the future, we plan to install the setup on our ion trap apparatus, and use it to engineer various types of spin-spin interactions between qubit spin states for future quantum simulation experiments, for example, simulating different types of 2D lattices[15].

# References

- [1] Jacob Biamonte, Peter Wittek, Nicola Pancotti, Patrick Rebentrost, Nathan Wiebe, and Seth Lloyd. Quantum machine learning. *Nature*, 549(7671):195, 2017.
- [2] Alexander Braun. *Addressing Single Yb<sup>138</sup> Ions: A New Scheme for Quantum Computing in Linear Ion Traps; [Experimente Durchgeföhrt Am Institut Für Laser-Physik Der Universität Hamburg]*. Cuvillier Verlag, 2007.
- [3] Juan I Cirac and Peter Zoller. Quantum computations with cold trapped ions. *Physical review letters*, 74(20):4091, 1995.
- [4] Shantanu Debnath, Norbert M Linke, Caroline Figgatt, Kevin A Landsman, Kevin Wright, and Christopher Monroe. Demonstration of a small programmable quantum computer with atomic qubits. *Nature*, 536(7614):63, 2016.
- [5] Jürgen Eschner, Giovanna Morigi, Ferdinand Schmidt-Kaler, and Rainer Blatt. Laser cooling of trapped ions. *JOSA B*, 20(5):1003–1015, 2003.
- [6] Alexander L Gaunt and Zoran Hadzibabic. Robust digital holography for ultracold atom trapping. *Scientific reports*, 2:721, 2012.
- [7] Richard Hauck and Olof Bryngdahl. Computer-generated holograms with pulse-density modulation. *JOSA A*, 1(1):5–10, 1984.
- [8] John F Jarvis, C Ni Judice, and WH Ninke. A survey of techniques for the display of continuous tone pictures on bilevel displays. *Computer graphics and image processing*, 5(1):13–40, 1976.
- [9] Dieter Just, Richard Hauck, and Olof Bryngdahl. Rational carrier-period for binarization of sampled images and holograms. *Optics communications*, 60(6):359–363, 1986.

- [10] Simcha Korenblit, Dvir Kafri, Wess C Campbell, Rajibul Islam, Emily E Edwards, Zhe-Xuan Gong, Guin-Dar Lin, Lu-Ming Duan, Jungsang Kim, Kihwan Kim, et al. Quantum simulation of spin models on an arbitrary lattice with trapped ions. *New Journal of Physics*, 14(9):095024, 2012.
- [11] Aaron C Lee, Jacob Smith, Philip Richerme, Brian Neyenhuis, Paul W Hess, Jiehang Zhang, and Christopher Monroe. Engineering large stark shifts for control of individual clock state qubits. *Physical Review A*, 94(4):042308, 2016.
- [12] Wai-Hon Lee. Binary computer-generated holograms. *Applied Optics*, 18(21):3661–3669, 1979.
- [13] Ben C Platt and Roland Shack. History and principles of shack-hartmann wavefront sensing. *Journal of refractive surgery*, 17(5):S573–S577, 2001.
- [14] MG Raizen, JM Gilligan, James C Bergquist, Wayne M Itano, and David J Wineland. Ionic crystals in a linear paul trap. *Physical Review A*, 45(9):6493, 1992.
- [15] Fereshteh Rajabi, Sainath Motlakunta, Chung-You Shih, Nikhil Kotibhaskar, Qudisia Quraishi, Ashok Ajoy, and Rajibul Islam. Dynamical hamiltonian engineering of 2d rectangular lattices in a one-dimensional ion chain. *npj Quantum Information*, 5(1):32, 2019.
- [16] Philipp Schindler, Daniel Nigg, Thomas Monz, Julio T Barreiro, Esteban Martinez, Shannon X Wang, Stephan Quint, Matthias F Brandl, Volckmar Nebendahl, Christian F Roos, et al. A quantum information processor with trapped ions. *New Journal of Physics*, 15(12):123012, 2013.
- [17] Marlan O Scully and M Suhail Zubairy. Quantum optics, 1999.
- [18] Peter W Shor. Algorithms for quantum computation: Discrete logarithms and factoring. In *Proceedings 35th annual symposium on foundations of computer science*, pages 124–134. Ieee, 1994.
- [19] Anders Sørensen and Klaus Mølmer. Quantum computation with ions in thermal motion. *Physical review letters*, 82(9):1971, 1999.
- [20] Daniel A Steck. *Quantum and atom optics*, volume 47. 2007.
- [21] Texas Instrument. *DLP9500UV DLP® 0.95 UV 1080p 2x LVDS Type A DMD*, 11 2014. REVISED MARCH 2017.

- [22] Ye Wang, Mark Um, Junhua Zhang, Shuoming An, Ming Lyu, Jing-Ning Zhang, L-M Duan, Dahyun Yum, and Kihwan Kim. Single-qubit quantum memory exceeding ten-minute coherence time. *Nature Photonics*, 11(10):646, 2017.
- [23] Robert C Weast, Melvin J Astle, William H Beyer, et al. *CRC handbook of chemistry and physics*, volume 69. CRC press Boca Raton, FL, 1988.
- [24] Frank Wyrowski. Iterative quantization of digital amplitude holograms. *Applied optics*, 28(18):3864–3870, 1989.
- [25] Wang Ye, Zhang Jing-Ning, and Kim Kihwan. Single-ion qubit with coherence time exceeding 10 minutes. *ACTA PHYSICA SINICA*, 68(3), 2019.
- [26] Philip Zupancic, Philipp M Preiss, Ruichao Ma, Alexander Lukin, M Eric Tai, Matthew Rispoli, Rajibul Islam, and Markus Greiner. Ultra-precise holographic beam shaping for microscopic quantum control. *Optics express*, 24(13):13881–13893, 2016.
- [27] Philip PJ Zupancic. Dynamic holography and beamshaping using digital micromirror devices. *LMU München, Grainer Lab Harvard*, 242, 2013.



# APPENDICES

# Appendix A

## Branching Ratio of D1 and D2 Line in $^{171}\text{Yb}^+$

To calculate AC Stark shift (section 3.4), we need to incorporate branching of D1 and D2 Line in  $^{171}\text{Yb}^+$ . To calculate the branching ratios for the sub-level Rabi frequencies  $\Omega$ , we will need to calculate all the components of dipole matrix elements. With Wigner-Eckart theorem, we can separate the angular dependencies of the dipole matrix element. The first term  $\langle F_e || \vec{d} || F_g \rangle$  is reduced dipole matrix element, and the second term  $CG_{F_g, m_g; 1, q}^{F_e, m_e}$  is the Clebsch-Gordan coefficient.

$$\langle F_e | d_q | F_g \rangle = \langle F_e || \vec{d} || F_g \rangle \langle F_e, m_e | F_g, m_g; 1, q \rangle = \langle F_e || \vec{d} || F_g \rangle CG_{F_g, m_g; 1, q}^{F_e, m_e} \quad (\text{A.1})$$

However, the quantum number  $F$  raises from the coupling of the net orbital angular momentum  $J$  and the nuclear spin  $I$ . The dipole operator  $\vec{d}$  refers to the position of the electron which couples to  $J$  only. As a result, we need to further processed the reduced dipole matrix element.

$$\langle F_e || \vec{d} || F_g \rangle = (-1)^{F_e + I + J_g + 1} \sqrt{(2F_g + 1)(2J_e + 1)} \left\{ \begin{matrix} J_g & J_e & 1 \\ F_e & F_g & I \end{matrix} \right\} \langle J_e || \vec{d} || J_g \rangle \quad (\text{A.2})$$

where the curly bracket  $\{...\}$  is the Wigner 6-j symbol.[20] For Ytterbium 171, the nuclear spin quantum number is  $\frac{1}{2}$ . With the definition of the Rabi frequency, we know the

Rabi frequency (proportional to the dipole matrix element) with polarization  $q$  will be:

$$\Omega^{(q)} = (-1)^{F_e + \frac{1}{2} + J_g + 1} \sqrt{(2F_g + 1)(2J_e + 1)} CG_{F_g, m_g, 1, q}^{F_e, m_e} \left\{ \begin{array}{ccc} J_g & J_e & 1 \\ F_e & F_g & \frac{1}{2} \end{array} \right\} g_0 \quad (\text{A.3})$$

$$= B_{F_g, m_g; 1, q}^{J_e, F_e, m_e} g_0 \quad (\text{A.4})$$

where  $g_0 = \Gamma^2 \frac{I_{laser}}{2I_{sat}}$  and  $B_{F_g, m_g; 1, q}^{J_e, F_e, m_e}$  is the branching ratio.  $\Gamma$  is the nature linewidth.  $I_{laser}$  is the intensity of the laser, and  $I_{sat}$  is the saturation intensity.

For D1 line transitions ( $^2P_{1/2}$  excited states), the non-zero branching ratios are:

$$B_{0,0;1,-1}^{1/2,1,-1} = -\frac{\sqrt{3}}{3} \quad (\text{A.5})$$

$$B_{1,0;1,-1}^{1/2,1,-1} = \frac{\sqrt{3}}{3} \quad (\text{A.6})$$

$$B_{1,1;1,-1}^{1/2,1,0} = \frac{\sqrt{3}}{3} \quad (\text{A.7})$$

$$B_{1,1;1,-1}^{1/2,0,0} = \frac{\sqrt{3}}{3} \quad (\text{A.8})$$

$$B_{0,0;1,0}^{1/2,1,0} = -\frac{\sqrt{3}}{3} \quad (\text{A.9})$$

$$B_{1,-1;1,0}^{1/2,1,-1} = -\frac{\sqrt{3}}{3} \quad (\text{A.10})$$

$$B_{1,0;1,0}^{1/2,0,0} = -\frac{\sqrt{3}}{3} \quad (\text{A.11})$$

$$B_{1,1;1,0}^{1/2,1,1} = \frac{\sqrt{3}}{3} \quad (\text{A.12})$$

$$B_{0,0;1,1}^{1/2,1,1} = -\frac{\sqrt{3}}{3} \quad (\text{A.13})$$

$$B_{1,-1;1,1}^{1/2,1,0} = -\frac{\sqrt{3}}{3} \quad (\text{A.14})$$

$$B_{1,-1;1,1}^{1/2,0,0} = \frac{\sqrt{3}}{3} \quad (\text{A.15})$$

$$B_{1,0;1,1}^{1/2,1,1} = -\frac{\sqrt{3}}{3} \quad (\text{A.16})$$

For D2 line transitions ( ${}^2P_{3/2}$  excited states), the non-zero branching ratios are:

$$B_{0,0;1,-1}^{3/2,1,-1} = \frac{\sqrt{6}}{3} \quad (\text{A.17})$$

$$B_{1,-1;1,-1}^{3/2,2,-2} = 1 \quad (\text{A.18})$$

$$B_{1,0;1,-1}^{3/2,2,-1} = \frac{\sqrt{2}}{2} \quad (\text{A.19})$$

$$B_{1,0;1,-1}^{3/2,1,-1} = \frac{\sqrt{6}}{6} \quad (\text{A.20})$$

$$B_{1,1;1,-1}^{3/2,2,0} = \frac{\sqrt{6}}{6} \quad (\text{A.21})$$

$$B_{1,1;1,-1}^{3/2,1,0} = \frac{\sqrt{6}}{6} \quad (\text{A.22})$$

$$B_{0,0;1,0}^{3/2,1,0} = \frac{\sqrt{6}}{3} \quad (\text{A.23})$$

$$B_{1,-1;1,0}^{3/2,2,-1} = \frac{\sqrt{2}}{2} \quad (\text{A.24})$$

$$B_{1,-1;1,0}^{3/2,1,-1} = -\frac{\sqrt{6}}{6} \quad (\text{A.25})$$

$$B_{1,0;1,0}^{3/2,2,0} = \frac{\sqrt{6}}{3} \quad (\text{A.26})$$

$$B_{1,1;1,0}^{3/2,2,1} = \frac{\sqrt{2}}{2} \quad (\text{A.27})$$

$$B_{1,1;1,0}^{3/2,1,1} = \frac{\sqrt{6}}{6} \quad (\text{A.28})$$

$$B_{0,0;1,1}^{3/2,1,1} = \frac{\sqrt{6}}{3} \quad (\text{A.29})$$

$$B_{1,-1;1,1}^{3/2,2,0} = \frac{\sqrt{6}}{6} \quad (\text{A.30})$$

$$B_{1,-1;1,1}^{3/2,1,0} = -\frac{\sqrt{6}}{6} \quad (\text{A.31})$$

$$B_{1,0;1,1}^{3/2,2,1} = \frac{\sqrt{2}}{2} \quad (\text{A.32})$$

$$B_{1,0;1,1}^{3/2,1,1} = -\frac{\sqrt{6}}{6} \quad (\text{A.33})$$

$$B_{1,1;1,1}^{3/2,2,2} = 1 \quad (\text{A.34})$$

# Appendix B

## Holographic Beam Shaping with Pulsed Laser

In a trapped-ion quantum simulator, it is common to do individual addressing with pulsed lasers. The main reason to use a pulsed laser is that we can use two comb teeth in the frequency domain to couple the two-qubit states. It saves the requirement of having two mode-lock lasers while performing Raman transition. Also, the pulsed laser can be used to generate differential fourth-order AC Stark shift.[11] Unlike the second-order AC Stark shifts shown in equation 3.22 and 3.23 that shift in the same direction, the fourth-order AC Stark shifts of the two-qubit states are shifted in the opposite direction. It may give us a larger phase shift with a sufficient amount of power.

However, there are extra things to consider while using holographic beam shaping on the pulsed laser. We know the position of the beam is wavelength dependent, and the short pulse width makes the frequency comb tooth spans over the frequency domain. To estimate the broadening of the beam profile from the effect, we first consider the separation between zeroth and n-th micro-mirror grating order is:

$$|\mathbf{x}_0^{(n)}| = n\sqrt{2}\frac{\lambda f}{D} \quad (\text{B.1})$$

where  $d$  is the edge length of the micro-mirror. The  $\sqrt{2}$  term comes from the fact that the mirror is flipping along the diagonal direction. The details of diffraction from micro-mirror grating is in section 3.3. The broadening results from the short pulse width gives us:

$$\delta x = n\sqrt{2}\frac{f}{d}\delta\lambda \quad (\text{B.2})$$

On the other hand, the diameter of the profile at the image plane  $D_i$  is roughly inverse proportional to the diameter at the Fourier plane  $D_f$ .

$$D_i = \frac{\lambda f}{D_f} \quad (\text{B.3})$$

The relation between wavelength  $\lambda$  and laser frequency  $\nu$  is:

$$\delta\lambda = \frac{\lambda}{\nu} \delta\nu \quad (\text{B.4})$$

The frequency span  $\delta\nu$  is basically one over the pulsed width. With equation [B.2](#), [B.3](#), and [B](#), we can get the ratio between  $\delta x$  and  $D_i$ .

$$r = \frac{\delta x}{D_i} = n\sqrt{2} \frac{D_f}{d} \frac{\delta\nu}{\nu} \quad (\text{B.5})$$

This ratio indicates the broadening relative to the size of the profile at the image plane. Below is the parameter of the laser used in our lab. Ideally we want to make it smaller than one. (The smaller the better) With  $n = 8$  and the parameter of the pulsed laser in our lab,

$$\nu = 844\text{THz} \quad (\text{B.6})$$

$$\delta\nu = 1/(15\text{ps}) = 67\text{GHz} \quad (\text{B.7})$$

$$D_f = 500d \quad (\text{B.8})$$

, we have  $r \approx 0.4$ . The number isn't much less than one. We might want to use a smaller  $n$  if we want to use the pulsed laser.